

Spatially Correlated Depth Changes in the Nearshore Zone During Autumn Storms

ALEX E. HAY

*Department of Physics and Ocean Sciences Centre, Memorial University of Newfoundland
St. John's, Canada*

ANTHONY J. BOWEN

Department of Oceanography, Dalhousie University, Halifax, Nova Scotia, Canada

Acoustic reflection measurements of seabed elevation were made at Stanhope Beach, Prince Edward Island, during three successive storms in October–November 1989. The instruments were located approximately 200 m offshore on the seaward face of a shore parallel bar in a mean water depth of 2.2 m. Bed elevation measurements were made at 30-min intervals with a range resolution of ± 1 mm at horizontal spacings between 22 cm and 1.5 m, using an array of four acoustic sounders operating at 1, 2.25, and 5 MHz. It is shown that such an array can be used as (1) an interferometer to determine bedform properties and migration rates, (2) a leveling device to determine changes in local bottom slope, and (3) an erosion/deposition gauge. In the interferometric mode, time domain autocorrelation and cross-correlation analyses of the bottom elevations are used to estimate the wavelengths, migration rates, and migration directions of sand ripples and megaripples. The ripple wavelengths (10–15 cm) and heights (3–5 cm) are comparable to measurements made by divers. Ripple migration rates were 1–6 cm h⁻¹ directed offshore in the direction of the mean shore normal near-bottom current and increased with increasing mean current speed. Evidence of megaripple-like features (2–5 cm height; 1.5–3 m length) is found, also migrating in the direction of the mean shore normal near-bottom drift, at speeds of about 20 cm h⁻¹. Bedload transport rates in the onshore-offshore direction are estimated from the bedform migration rates. The ripple transport rate was small (an order of magnitude smaller than the transport of sediments in suspension by the mean offshore drift). In contrast, the large-scale bedform transport appears to have been comparable to the mean current transport of suspended sediment. Interestingly, it appears that the total bedform transport was comparable to that predicted by Watanabe's (1981) net bedload transport formula, provided a coefficient appropriate to irregular wave conditions is used. During the third and highest-energy storm event, the measurements indicate transition to flat bed, and generalized local erosion at a maximum rate of 8 cm h⁻¹. This erosion event was associated with a general shoreward migration of the bar.

1. INTRODUCTION

It has proved difficult to monitor the morphological evolution of the seabed in nearshore environments during storm conditions. As stated by Allen [1982, p. 450] in his extensive treatment of sedimentary structures, "practical difficulties have held back knowledge of the surface and internal structures of submerged bars and troughs. . . ." These practical difficulties are associated with high velocity wave orbital motions and longshore currents, which not only impose severe constraints on instrumentation and data transmission both through the directly imposed forces on instrument platforms and cables, but also stir up material from the bottom, which is consequently obscured from view. The information available on the distribution of bedforms beyond the intertidal zone has as a result been restricted for the most part to that obtainable in relatively calm conditions by diving [Inman, 1957; Clifton *et al.*, 1971; Davidson-Arnott and Greenwood, 1976; Hunter *et al.*, 1979; Greenwood and Mittler, 1979; Miller and Komar, 1980]. A notable exception is the acoustic profiling measurements of sand ripples in the nearshore by Dingler [1974]. Internal sedimentary structures found in core samples taken from submerged bars [Davidson-Arnott and Greenwood, 1976; Hunter *et al.*, 1979;

Greenwood and Mittler, 1979] have been interpreted qualitatively in terms of bedform type and bedform migration direction. While this approach provides essential links to the geological record, it is limited in that one cannot be entirely certain of the sequence of events that occurred during a storm on the basis of the preserved signatures, and quantitative estimates of sediment transport rates cannot be made.

Bedforms represent a critical component of the sediment transport problem, both because bedform migration can provide a means of quantifying the bedload component of the total sediment transport [e.g., Dyer and Soulsby, 1988] and, more fundamentally, because of the coupling through bottom friction between the bedforms and the fluid motions [e.g., Grant and Madsen, 1986]. Although the practical difficulties cited above have continued to limit our knowledge of bedform development beyond the intertidal zone, significant advances have taken place over the past decade in the development of fast response optical and acoustic instrumentation for quantitative measurements of sediments in suspension [Downing *et al.*, 1981; Young *et al.*, 1982; Hess and Bedford, 1985; Lynch *et al.*, 1987; Hay *et al.*, 1988; Hanes *et al.*, 1988; Lynch and Agrawal, 1991; Thorne *et al.*, 1991; Hay and Sheng, 1992]. The results obtained with these sensors are beginning to confirm the expected importance of the interaction between bedforms and suspended sediment dynamics. For example, Vincent *et al.* [1991] have shown that changes in the shape of the vertical profile of suspended

Copyright 1993 by the American Geophysical Union.

Paper number 93JC00452.
0148-0227/93/93JC-00452\$05.00

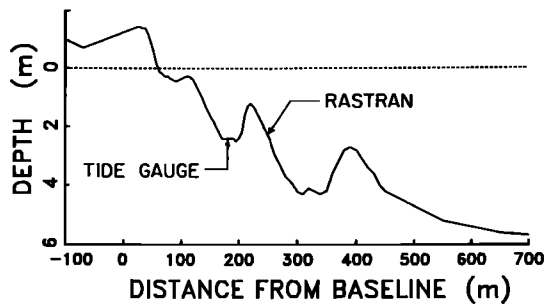


Fig. 1. Beach profile, showing location of the RASTRAN frame and the tide gauge.

sediment concentration with time may be associated with changes in ripple properties. Direct measurements of ripple geometry were not available to confirm this suggestion, however.

In this paper we present measurements of the morphological development of the seabed on horizontal scales of $O(10\text{ cm})$ to $O(1\text{ m})$ during three autumn storms. The measurements were made on the seaward face of a linear bar consisting of fine to medium sand, and were made acoustically. Our intention is first to demonstrate that the elevation of the seabed can be determined to within a few millimeters using megahertz-frequency acoustic backscatter from heights above bottom of $O(1\text{ m})$ during storm conditions in the nearshore. We then use these measurements to study the local time evolution of the seabed, including the development and migration of bedforms, during the three storm events.

The presentation of results begins with a summary of the hydrodynamic and bed elevation measurements for the three storms. This documents the time course of the forcing, and the response of the bed. In our discussion of the seabed response, we find it useful to separate the observed bed elevation changes into high- and low-frequency components. Low-frequency changes in bed elevation are defined to be those occurring on time scales of several hours to a few days. High-frequency bed elevation changes occur on time scales of a few hours or less. The changes in the low-frequency range (days) are checked against independent measurements of elevation made by scuba divers between storms, and with leveling rod surveys of the local bottom slope.

We then proceed with the analysis of the high-frequency bed elevation changes. It is argued that these variations are mainly due to sand ripples migrating through the measurement region. The argument proceeds as follows. First, the amplitude of these variations is found to be typical of diver measurements of ripple amplitudes between storms. Second, these amplitudes vary during a storm in a manner consistent with the criteria, based upon the nondimensional bottom stress [e.g., Nielsen, 1981; Sleath, 1984; Horikawa, 1988], for the existence of ripples in the presence of waves. Third, the array of acoustic sounders is an interferometer, and lagged correlation analysis in the time domain of bed elevations from the different sounders in the array yields estimates of the ripple wavelengths. These wavelengths agree well with those measured by divers between storms, and the wavelengths and steepnesses are in the range expected for wave ripples for the wave conditions encountered during the

experiment. The interferometric method also yields estimates of ripple migration velocities. Finally, evidence is presented which indicates that on two occasions large-scale bedforms, which we presume to be megaripples, propagated through the array. The ripple and megaripple migration rates lead to estimates of the bedload transport, and to comparisons with the suspended sediment transport, and with bedload transport formulae. We begin with a brief description of experimental methods.

2. EXPERIMENTAL METHODS

The data were collected at Stanhope Lane Beach with remote acoustic sediment transport (RASTRAN) system 1 [Hay et al., 1988; Hay, 1991]. Figure 1 shows the location of the RASTRAN frame on the seaward face of the second bar, 200 m offshore in a mean water depth of 2.2 m. The bottom sediments at the RASTRAN location consisted of unimodal sand with a median grain diameter of $170\ \mu\text{m}$, distributed lognormally about the geometric mean with a logarithmic standard deviation of about 1.25.

Figure 2 shows the RASTRAN frame itself, and the locations of the different sensors on the frame. Horizontal velocity measurements were made with Marsh-McBirney electromagnetic (em) flow meters. The em flow meters were sampled at a rate of 4.55 Hz using the UDATS underwater data acquisition system [Hazen et al., 1987]. Temperature and mean water level were recorded by a tide gauge located in the nearshore trough (Figure 1). The mean water levels at

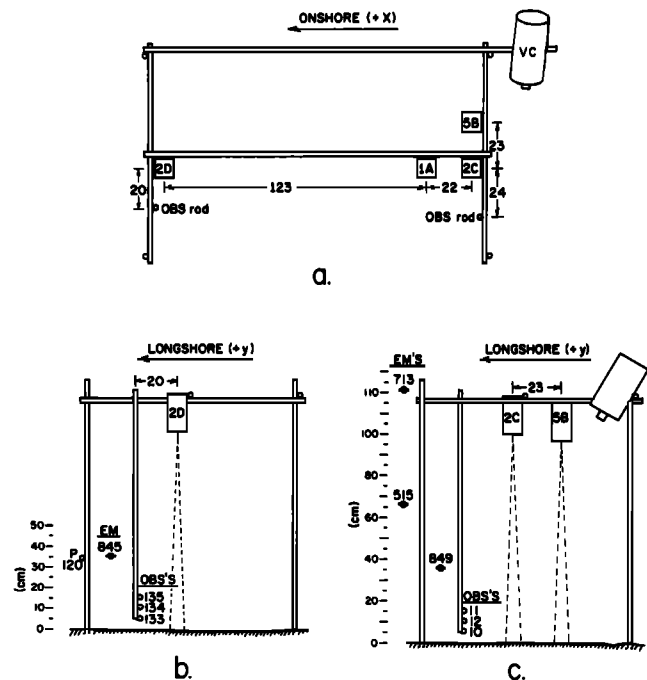


Fig. 2. The RASTRAN frame in (a) top view and (b) landward and (c) seaward end views, looking shoreward. The frame is shown to scale and was constructed from 2.5-cm-diameter stainless steel rod, clamped at the corners. The corner posts were flanged at the base, and the bases were buried to a depth of $O(0.5\text{ m})$. Guy wires were strung from the tops of the corner posts to buried anchors positioned 5 m to the sides and were made taut with turnbuckles. The acoustic sounder designations indicate frequency: that is, 1A = 1.00 MHz, 5B = 5.0 MHz, and 2C, 2D = 2.25 MHz. VC = video camera.

the RASTRAN location were determined from the tide gauge measurements using survey data taken along the instrument line between storms. Also shown on the RASTRAN frame is a video camera, which was also cabled to shore. It was possible to obtain good quality video imagery of the bottom, allowing bed features to be resolved, only during periods of relative calm between storms, or during the early or dying stages of a storm. During periods of peak storm activity, the bottom was generally obscured by light scattering from fine material in suspension.

The acoustic sounders used with RASTRAN system 1 are Mesotech model 810 units operating at 1, 2.25, and 5 MHz. Three of these units were mounted in a cluster at the seaward end of the frame, separated by 22–23 cm in the horizontal (Figure 2). A fourth was mounted at the opposite end, about 1.5 m shoreward. The acoustic pulses in this experiment were transmitted at a rate of 100 Hz and were 20 μ s in duration. The beamwidths for all units are about 4° (full width between half-power points). All units were at a nominal height above bottom of $O(1$ m), and therefore insonified an area of the seabed about 7 cm in diameter (Figure 2). The signals from the different sounders were envelope-detected, with a custom-built 100 kHz bandwidth detector [Hay, 1991]. For the distance to bottom measurements reported here, the signal envelopes were routed to a digital oscilloscope sampling at 1 MHz and triggered simultaneously with the acoustic sounders. The distance to bottom was obtained from the posttrigger arrival time of the bottom echo and from the speed of sound. The arrival time of the bottom echo (the leading edge of the echo) was determined from the oscilloscope trace to within ± 1 μ s.

In practice, the shape of the bottom echo was found to be highly variable from pulse to pulse, presumably because of the effects of time-varying sediment motion at the bed. This was true even under relatively quiescent conditions (small-amplitude, long-period swell). From the video observations it was clear that platelike pieces of shell hash resting on the bottom were flipped from side to side at these times, and very likely contributed to the bottom echo variability. In order to obtain a consistent and objective measure of bottom echo arrival time, minimally affected by time-varying suspended sediment concentrations, only those echoes meeting the following conditions were accepted: (1) detector saturation, so that the bottom echo was strong enough to saturate the receiver, (2) detector saturation lasting at least the duration of the transmitted pulse, and (3) backscatter amplitudes from suspended sediment above the bottom less than half the saturation amplitude. An echo satisfying this three-level criterion was captured to obtain the arrival time, which was then checked by allowing the oscilloscope to trigger freely again to ensure that no similar echo arrived at a shorter time. In this way it was usually possible to obtain a measurement for one sounder in a minute or less, and on all four sounders in less than 5 min at the beginning and end of each half-hour data run. Because the leading edge of the bottom echo defined in this way was steep, the echo was resolved to within the sampling interval of the scope (1 μ s), better than 1 mm in range.

The dependence of the speed of sound on temperature and salinity variations potentially affect the accuracy of the bed elevation measurements. Salinity was monitored by collecting bucket samples at the shoreline. Temperature was monitored by the tide gauge. The mean water temperature during

the experiment was about 8.5°C. For our purposes, ± 2 mm represents an acceptable error in bottom position. At a mean temperature of about 9°C, the speed of sound varies approximately as 3.7 m s⁻¹ °C⁻¹, and 1.3 m s⁻¹ psu⁻¹ [MacKenzie, 1981]. A 2-mm error at 1 m range would require a 3 m s error in the speed of sound and therefore a 0.8°C change in temperature or a 2.3 psu change in salinity. Such large changes were not generally observed during the experiment. The mean salinity was 29.1 psu, ± 0.2 psu standard deviation. During the first two storms, the mean temperature was the same, 8.9°C, $\pm 0.26^\circ$ standard deviation for the first storm, and $\pm 0.15^\circ$ C for the second storm. Maximum departures from the mean did not exceed 0.6°C. For the third storm, temperatures ran between 9.5° and 8.5°C during the first 2.5 days and then dropped steadily to 7.5°C on the last half day. These changes are tolerable at the ± 2 -mm level, with the exception of the temperature drop at the end of the third storm, which does not affect the results presented here, as will be seen. The bed elevations were therefore computed using a constant sound speed of 1476 m s⁻¹, corresponding to 8.5°C and 29.0 psu.

We briefly comment on the effects of the finite widths of the acoustic beams in relation to the measurement of sand ripple properties. Our principal objective was to determine the distance to the ripples when the crests and troughs were directly beneath the transducers. For sand lognormally distributed about a 170- μ m-diameter mean, the seabed should have been moderately rough at MHz acoustic frequencies according to the Rayleigh criterion [Ogilvy, 1991], using the 200- μ m width of the size distribution as a measure of the geometric surface roughness. One should therefore expect that for any given ripple migrating through the array, the distance to bottom determined in the manner described above would reach a minimum when the ripple crest was located directly beneath the transducer. Similarly, the strongest echo at maximum distance to bottom should occur at the ripple trough, provided the ripple wavelength is not less than the beamwidth. As will be shown, the wavelengths of the ripples at the RASTRAN location were $O(10$ cm). This is comparable to the 7-cm transducer beamwidths. It is therefore to be expected that some smoothing of the ripple profiles must have occurred.

3. RESULTS

We present below the distance to bottom and hydrodynamic measurements for each of the three storms. The horizontal coordinates and velocity components are defined as follows: x and u are the shore normal coordinate and velocity component respectively, with u positive onshore; y and v are shore parallel and positive to the left when looking shoreward.

3.1. Storm 1

The bed elevation measurements during the first storm are plotted in Figure 3. These are presented as distances-to-bottom from the individual transducers, or range, and therefore represent negative bottom elevations with respect to the frame.

The data are shown in raw form in Figures 3a and 3b and after being low-pass filtered with a 6-hour running average in Figure 3c. Throughout much of the record there is a vertical offset between the bottom distances obtained from the

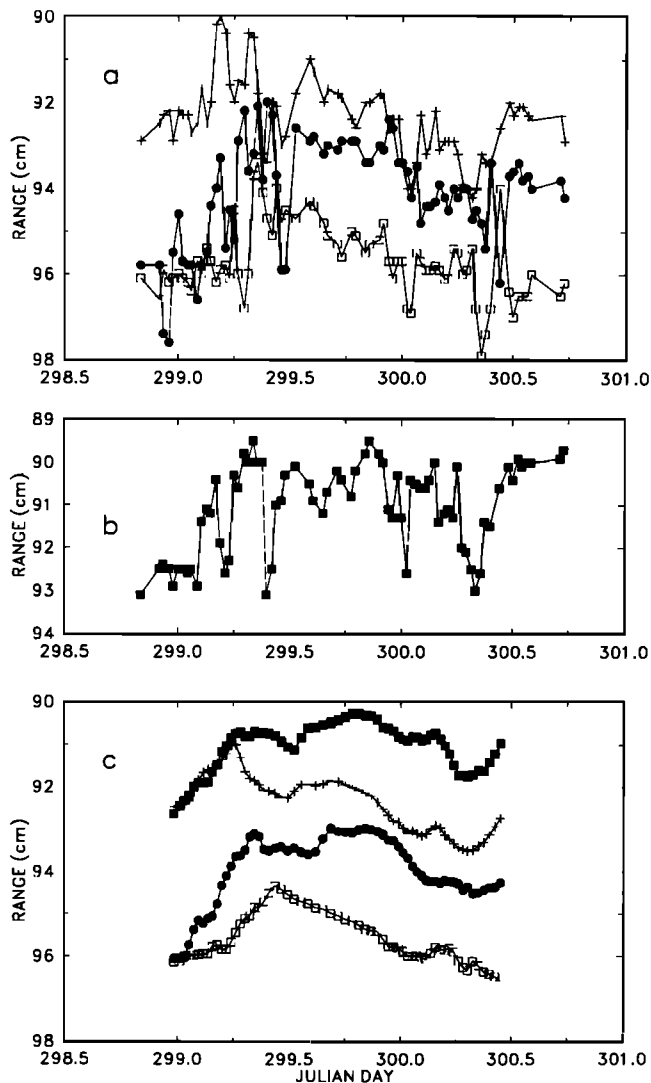


Fig. 3. Storm 1 distance to bottom, or (negative) bed elevation, time series. Figures 3a and 3b show the raw data; Figure 3c shows the low-passed data (6-hour running mean). The different symbols represent data from the different sounders: 1A, solid circles; 2c, open squares; 5B, pluses; and 2D, solid squares.

different sounders. This is most clearly visible in Figure 3c and is due to the different heights of the transducers above the sloping bed and to the fact that the transducers are not all at the same level below the frame: that is, the 5B transducer is about 2 cm farther below the frame than the other three (Figure 2). The low-pass-filtered bottom positions for this unit are generally about 2 cm less than those determined from sounder 2C, its nearest neighbor in the along-isobath (longshore) direction. Sounders 2C, 1A, and 2D, on the other hand, were suspended at the same levels on the frame but at points successively closer to shore. The mean slope in the on-offshore direction at the position of the RASTRAN frame was about 1:20 (Figure 1). Therefore the fact that the bottom positions registered by sounders 1A and 2D are 1–2 cm and 4–6 cm less, respectively, than those obtained from 2C, as shown by Figure 3c, is to be expected.

The measurements exhibit variability at both high and low frequencies, with amplitudes of a few centimeters in both cases. To reiterate, by low frequency we mean the variabil-

ity at periods of several hours or longer that are retained after low-pass filtering the data, characterizing changes in the mean position of the bed. The low-frequency changes registered by the different sounders are clearly correlated (Figure 3c). The high-frequency variations are those filtered out by the 6-hour running average and correspond therefore to variations on time scales of minutes to several hours. The high-frequency variations can be seen by comparing the filtered and unfiltered data in Figure 3. While perhaps not obvious from Figure 3, these variations are also correlated and, as we will show, are due to sand ripples migrating beneath the array.

The corresponding hydrodynamic forcing for the same period is presented in Figure 4. Figure 4a shows the rms onshore and alongshore components of velocity as registered by all three flow meters. These rms velocities were computed after removing the means for each half-hour data run, and therefore represent the shore normal and shore

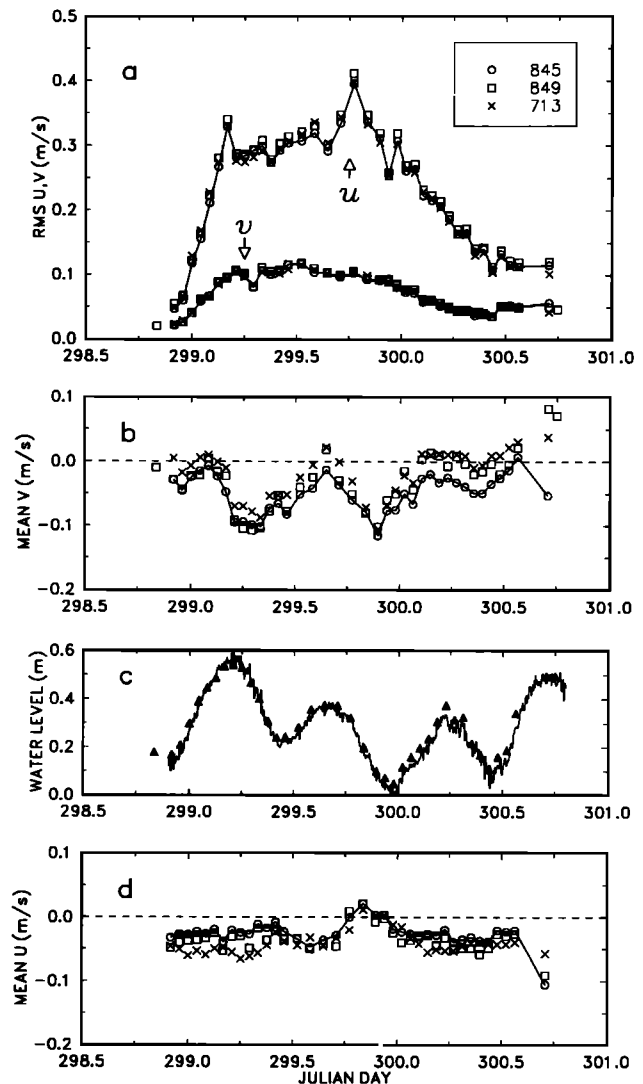


Fig. 4. Storm 1 hydrodynamic data: (a) the cross-shore u and alongshore v components of the rms wave orbital velocity, (b) the mean longshore current, (c) the sea level variations from the tide gauge and a pressure sensor on the bar crest (solid triangle), and (d) the mean cross-shore current. The symbols in Figures 4a, 4b, and 4d represent the different flow meters, as shown in the key, and the solid lines connect the points for flow meter 845 (arbitrary choice).

parallel components of the rms wave orbital velocity amplitude at the sensor position. The growth and decay of wave amplitude during the course of the storm is evident in both velocity components. The alongshore component was generally about a third of the onshore component, indicating that the angle of wave attack was within 20° of shore-normal. The alongshore current, shown in Figure 4b, reached maximum amplitudes of $O(10)$ cm s⁻¹. The changes in mean water level are shown in Figure 4c and can be seen to be largely tidal. Comparing Figures 4b and 4c, a pronounced modulation of the longshore current by the tide is apparent. Figure 4d shows the mean velocity in the shore-normal direction, which was small (usually about 5 cm s⁻¹ or less), and generally directed offshore at all three sensors.

3.2. Storm 2

The data set for the second storm is presented in Figures 5 and 6. Figure 5 shows the distance to bottom results. As for the first storm, both high- and low-frequency variations are

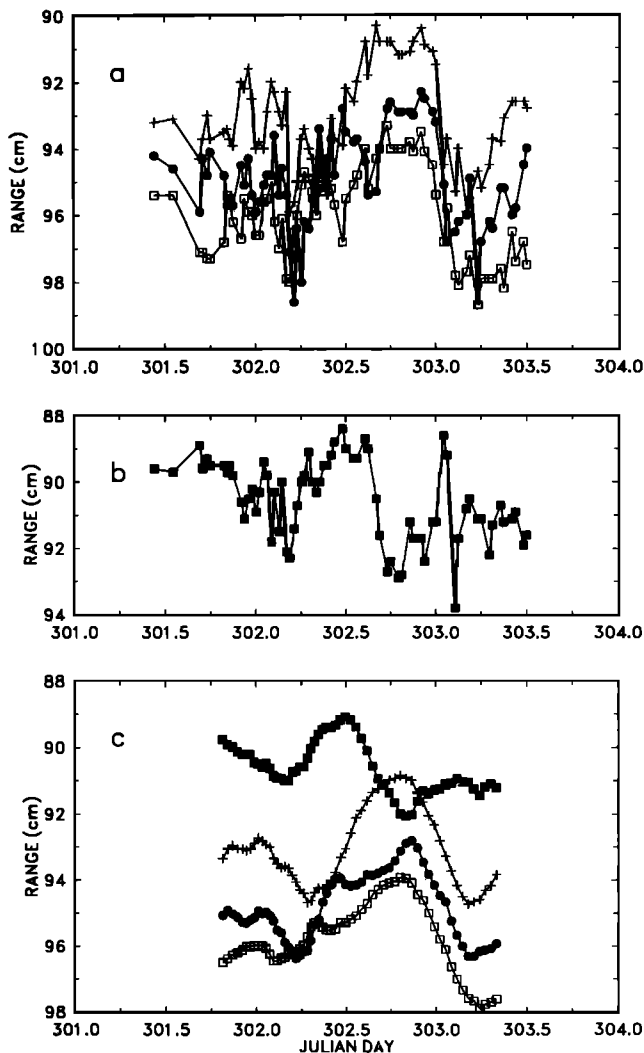


Fig. 5. Storm 2 bed elevation time series. Figures 5a and 5b show the raw data; Figure 5c shows low-passed data (6-hour running mean). As in Figure 3, the symbols represent the different sounders: 1A, solid circles, 2C, open squares; 5B, pluses; and 2D, solid squares.

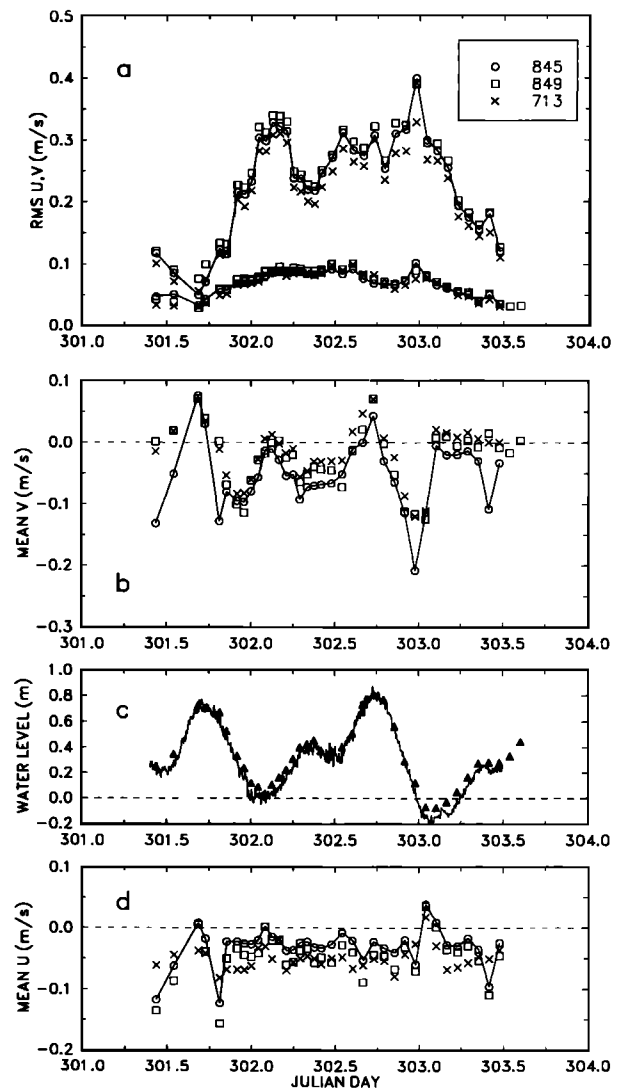


Fig. 6. Storm 2 hydrodynamic data: (a) the cross-shore u and alongshore v components of the rms wave orbital velocity, (b) the mean longshore current, (c) the sea level variations from the tide gauge and a pressure sensor on the bar crest (solid triangle), and (d) the mean cross-shore current. The symbols and solid lines in Figures 6a, 6b, and 6d are defined as in Figure 4.

present, as are vertical offsets between the records for the different sounders. These offsets are as before most easily distinguished in the low-passed data. For this storm, however, the phasing of the low-frequency changes is distinctly different at opposite ends of the frame. Between Julian day (JD) 302.5 and JD 303 at the offshore end, for example, all three sounders in the three-frequency cluster registered a period of decreasing bottom range followed by increasing bottom ranges, resulting in a maximum in bed elevation at JD 302.8. At the other end of the frame, the changes in bed elevation were phase-shifted by roughly 90°; that is, increasing ranges early in the time period followed by decreasing ranges later resulted in a minimum in bed elevation at JD 302.8. The peak-to-peak variation was 3–4 cm. These changes might suggest no overall net transport of material in the onshore-offshore direction, that is, initial erosion of material from the landward end of the frame to be deposited seaward, followed by erosion at the seaward end accompa-

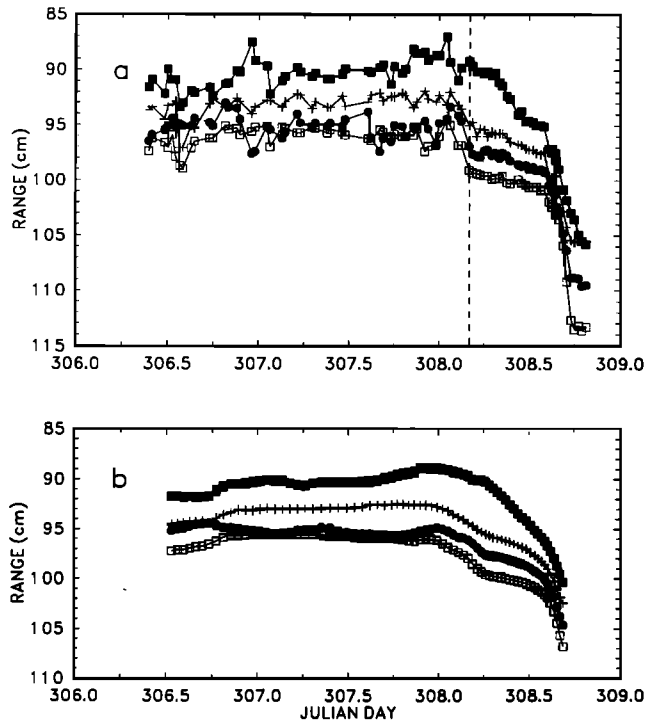


Fig. 7. Storm 3 bed elevation time series. Figure 7a shows the raw data; Figure 7b shows the low-passed data. As in Figures 3 and 5, the symbols represent the different sounders: 1A, solid circles; 2C, open squares; 5B, pluses; and 2D, solid squares. The vertical dashed line in Figure 7a denotes the transition to flat bed on JD 308.17 (see text).

nied by deposition landward and a return to the initial bed configuration. Another possible explanation involves a large-scale bedform migrating under the frame. This question will be pursued later. In either case, on JD 302.8 the net effect is a pronounced reduction in the mean bottom slope in the on-offshore direction along the length of the frame, to 1:75 from 1:25 initially. As in storm 1, high-frequency variations in the bottom elevations of 2–3 cm maximum amplitude can be seen by comparing the low-passed and unfiltered data.

The rms wave orbital velocities are presented in Figure 6. Again, the longshore component during the main part of the storm was about 0.25–0.33 of the shore normal component, indicating angles of wave attack less than 20°. The maximum rms velocities in the shore normal direction were 0.3–0.4 m s⁻¹, comparable to those reached during storm 1. The longshore current (Figure 6b) was at times stronger than in storm 1, with peak values approaching 15–20 cm s⁻¹. The mean sea surface elevation time series is shown in Figure 6c. A strong tidal signal is present and is dominantly diurnal. The tidal variations in water level are again clearly reflected in the longshore current data. The mean shore normal velocities (Figure 6d) were again directed mainly offshore, with 5 cm s⁻¹ being a typical speed.

3.3. Storm 3

The time series of bottom distances during the third storm are presented in Figure 7. Figure 8 shows the velocity and water level measurements. It is immediately apparent from both figures that this storm was different from the previous two. During the latter part of the storm (after JD 308.5) the

longshore current rapidly increased in strength, approaching speeds of 40 cm s⁻¹ (Figure 8b). This is much stronger than the 10–15 cm s⁻¹ maximum speeds generated in storms 1 and 2. (Note that at both the beginning and end of the storm 3 record, when the longshore current was strongest, the waves attacked the beach more obliquely than during storms 1 and 2: Figure 8a indicates angle of attack greater than 25°). The maximum rms wave orbital velocities reached values of 0.4–0.5 m s⁻¹, larger than in the first two storms. As in storms 1 and 2, the mean shore normal velocities (Figure 8d) were generally small (5 cm s⁻¹ or less) and directed offshore, except at the end of the record during the period of strong longshore flow, when the data indicate shoreward mean flow near the bed, and seaward flow above.

The distances to bottom (Figure 7) exhibit two features not encountered during the other storms. One is the pronounced and rapid decrease in bed elevation, essentially simultaneous at both ends of the frame, beginning at about JD 308.6. This coincided with a sharp increase in the wave forcing (Figure 8a), and occurred during the time of rapid growth in the longshore current (Figure 8b). The bed level dropped by 12

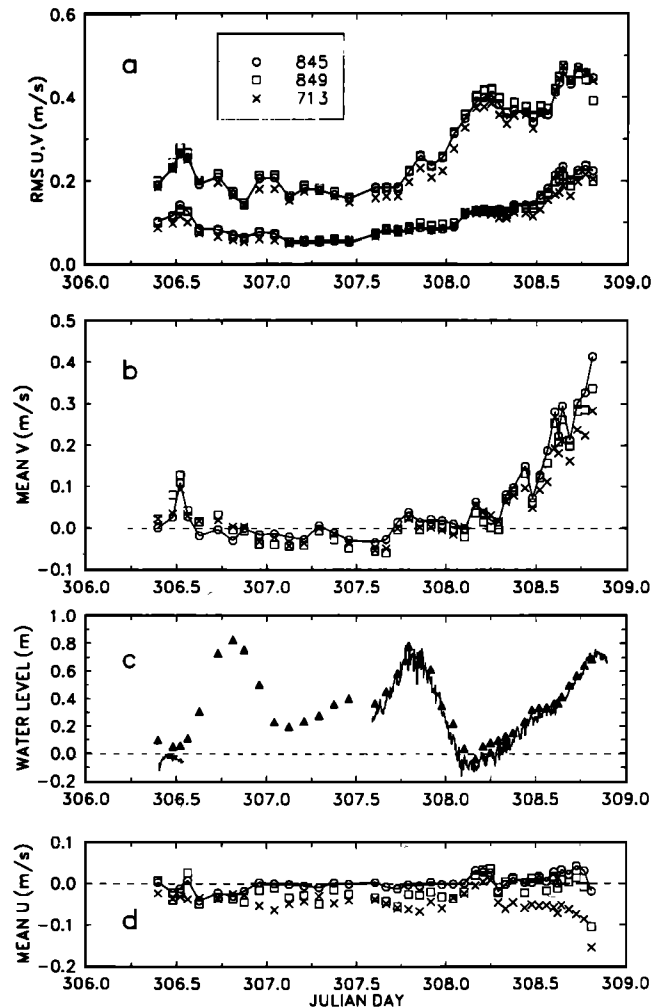


Fig. 8. Storm 3 hydrodynamic data: (a) the cross-shore u and alongshore v components of the rms wave orbital velocity, (b) the mean longshore current, (c) the sea level variations from the tide gauge and a pressure sensor on the bar crest (solid triangle) and (d) the mean cross-shore current. The symbols and solid lines in Figures 8a, 8b, and 8d are defined as in Figure 4.

cm in 3.5 hours. The maximum depression rate was about 8 cm h⁻¹. That this drop in bed level occurred at the same time and with the same amplitude at both ends of the frame, and under conditions of strong longshore flow and large wave orbital velocities, suggests generalized local erosion. This erosion was later confirmed by diver observations made subsequent to the storm on JD 310, which indicated that the entire bar had migrated shoreward.

The other feature of interest in the bottom distance data in Figure 7 is the disappearance of the ripple signature (high-frequency, centimeter-scale variations) during the latter part of the record, prior to the onset of rapid erosion. At JD 308.17 in Figure 7a, the time series for all four sounders exhibit distinct decreases in the amplitude of the high-frequency variations. During the earlier part of the record, high-frequency fluctuations with amplitudes of several centimeters peak to peak are evident. These fluctuations are similar in amplitude to those observed during the first two storms (Figures 3 and 5) and coincide with the period of low current and low wave amplitudes in the first part of the storm (Figure 8). At JD 308.17, however, when the reduction in the high-frequency variations began, the rms wave orbital velocities and longshore current were increasing. We argue below that the reduced amplitudes are caused by transition to flat bed.

Finally, referring to the unfiltered data in Figure 7a, a rapid depression of the seabed with 5-cm amplitude occurred beneath all three sounders at the seaward end of the frame immediately prior to the flat bed transition at JD 308.17. A similar depression occurred beneath the fourth sounder (2D) 1.5 m landward, but some 6 hours later. It is tempting to believe that these features are related, in which case they might be caused by a large-scale bedform propagating through the array. This interpretation of Figure 7 would indicate a landward velocity component of about 24 cm h⁻¹ for this bedform.

3.4. Mean Bottom Position: Comparison With Diver Measurements

The low-frequency changes in mean bottom position can be compared with scuba diver observations. Diver measurements of distance-to-bottom were made between storms, using a hand-held measuring tape. The diver and acoustic

TABLE 1. Mean and Standard Deviation in the Difference Between Distance to Bottom Measurements Made by Divers and With RASTRAN

Sounder	Difference, cm
1.00A	0.6 ± 0.4
2.25C	1.7 ± 0.5
5.00B	0.3 ± 0.9
2.25D	0.9 ± 0.7

See also Figure 9.

measurements are compared in Figure 9. The mean differences and standard deviations are listed for each sounder in Table 1. The acoustic measures of bed elevation are consistently offset to larger values in the mean by about 0.5–1.5 cm, or about 1–2%. This offset cannot be attributed to any delay time unaccounted for in the acoustic measurement, as the range determination method was tested in the laboratory using the same cabling configuration as used in the field.

Figure 9 confirms the use of the acoustic sounder array for mean local bottom slope measurement. From the data in Figure 9, the mean bottom distances at the two 2.25-MHz unit locations at opposite ends of the frame are: from RASTRAN, 96.2 ± 0.7 cm and 91.2 ± 1.2 cm at the seaward and landward ends, respectively, and from the diver measurements, 94.5 ± 1 cm and 90.2 ± 1.3 cm. The scatter in these measurements is comparable to the amplitudes of sand ripples and is partly attributed to their presence. The end-to-end difference in the mean values is 5.0 cm for RASTRAN and 4.3 cm for the diver measurements. These values are quite comparable. The acoustic mean difference gives a mean bottom slope along the length of the frame of 1:29, which is consistent with the slope of the seaward face of the bar (Figure 1).

3.5. Ripple Amplitudes and Transition to Flat Bed

The high-frequency variations in bottom position during each of the three storms are shown in Figure 10. The peak-to-peak amplitudes are of the same order for all three storms: about 2–5 cm. These values are comparable to the range of sand ripple heights measured at the RASTRAN frame location by divers between storms (Table 2) and are the first point in our argument that the high-frequency variations are the result of ripple development and migration.

The rms amplitudes of the high-frequency variations change considerably with time. This can be seen, for example, at the end of the third storm (Figure 10c), when the variations registered by all four sounders drop to less than 2–3 mm rms amplitude, which approaches the probable noise level of our bed elevation measurements. This period of reduced variation follows what we have called the transition to flat bed at JD 308.17. It is not the only period of low-amplitude variation to have occurred during the three storms, however. Shorter periods of low variability are found in the data for storm 1 (JD 299.5–300.25, Figure 10a), and for storm 2 (JD 302.75–303, Figure 10b).

For sandy sediments of a given mean size, the properties of wave-generated ripples depend upon the magnitude of the Shields bottom stress parameter [e.g., Nielsen, 1981]

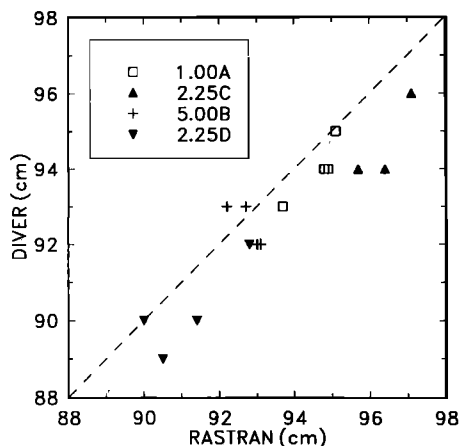


Fig. 9. Diver and RASTRAN distance to bottom measurements. The data for the different sounders are identified in the key.

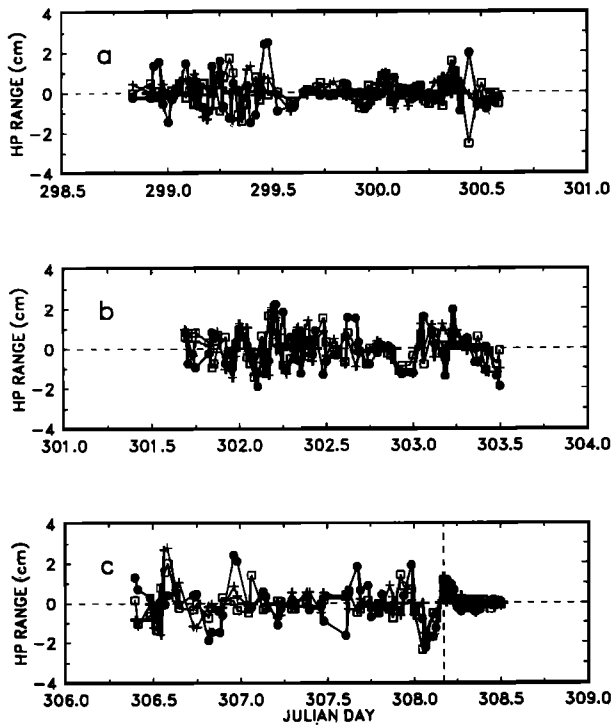


Fig. 10. High-frequency distance to bottom variations during (a) storm 1, (b) storm 2, and (c) storm 3. Symbols identifying the different sounders are as in Figures 3, 5 and 7. The vertical dashed line in Figure 10c denotes the transition to flat bed on JD 308.17.

$$\psi = f_w u_b^2 / 2(s - 1)gD, \quad (1)$$

which is the maximum bottom shear stress during a wave cycle, nondimensionalized by the grain buoyancy. D is the median grain diameter of the bottom sediments, g is the acceleration due to gravity, s the specific gravity of the grains, u_b is the maximum near-bottom wave orbital velocity, and f_w is a wave friction factor.

Wave ripples occur between upper and lower threshold values of ψ . The lower bound is determined by the threshold of grain motion, which is dependent on grain size, and for sediments with diameter $D = 170 \mu\text{m}$ and $s = 2.7$ (quartz) it is about 0.7 at water temperatures near 10°C [Madsen and Grant, 1977; Horikawa, 1988, p. 180; Kraus and Horikawa, 1990]. The upper bound corresponds to the transition to flat bed and occurs at about $\psi = 0.8$ [Nielsen, 1979, 1981; Sleath, 1984, p. 145; Horikawa, 1988, p. 181]. The upper bound appears to be approximately independent of grain size [Horikawa et al., 1982; Horikawa, 1988, p. 181]. It should be emphasized that these threshold criteria are based mainly on laboratory experiments made using regular waves. An exception is Nielsen's [1981] study, which showed using field data from Inman [1957] and Dingler [1974] that these criteria could also be applied to field conditions (i.e., irregular waves), provided that the Shields parameter was computed using the significant wave orbital velocity.

The wave friction factor f_w was computed here using the Jonsson [1966] formula

$$\frac{1}{4\sqrt{f_w}} + \log_{10} \frac{1}{4\sqrt{f_w}} = -0.08 + \log_{10} \frac{a}{k_N}, \quad (2)$$

where k_N is the Nikuradse grain roughness, taken to be 2.5 times the median grain diameter following Nielsen [1981] (see also Sleath [1984, p. 39]). (Friction factors were also computed using the Nielsen [1981] approximation to (2), with essentially identical results.) The parameter a is the near-bottom wave orbital amplitude, taken here from linear shallow water wave theory to be given by $u_b T_p / 2\pi$, where T_p is the period at peak wave energy spectral density and u_b is the significant wave orbital velocity computed from the near-bottom current meter measurements. Specifically, u_b is taken to be $2u_{\text{rms}}$, where u_{rms}^2 is the variance of the u time series, corresponding to a Gaussian distribution of sea surface elevations [e.g., Guza and Thornton, 1980]. We note that the friction factors computed in this way represent minimum estimates, as the effects of wave-current interaction [Grant and Madsen, 1979], leading to increased apparent bottom roughness, are not included. The justification for this is that during the periods of greatest interest, the mean currents were weak relative to the wave motions: 20–30% of u_{rms} and therefore 10–15% of the significant wave orbital velocities.

Figure 11 shows the frequency of the main spectral peak for each storm. Wave periods were typically in the 4–6 s range during each of the first two storms. The longest period waves, with T_p reaching 8 s, occurred midway through the second storm, and frequently during the third storm.

The computed friction factors (not shown) fall mostly in the range 0.007–0.012, and differ little among the storms, except under low-energy conditions during the early stages. At these times the combined modulation by wave amplitude and peak period leads to 50% or larger variations in f_w . After this initial period, however, the forcing levels off and the variations in the f_w estimates are much reduced. As a result, the Shields parameter (shown for each storm in Figure 12) essentially follows the envelope of the shore normal orbital velocities (Figures 4, 6, and 8). Also shown in Figure 12 as horizontal dashed lines are the lower and upper bounds on ψ defining the wave ripple existence region.

Comparing Figure 12 with the high-frequency bottom position variations in Figure 10, one immediately sees a direct correspondence between reductions in the amplitudes of the bottom position variations, and those times at which the flat bed criterion is approached or exceeded. For example, during storm 3, the transition on JD 308.17 to what we previously identified as flat bed conditions on the basis of the bed elevation measurements alone (Figures 7a and 10c), is confirmed by the shear stress estimates in Figure 12c. These estimates show that the stress exceeded the flat bed limit shortly before JD 308.17 and remained above it afterward. Similarly, during storm 1 the flat bed limit was exceeded near JD 299.8 (Figure 12a), a time at which bottom position variations were at a minimum for that storm (Figure 10a).

TABLE 2. Ripple Characteristics From Diver Observations

JD	Approximate Time, LT	Height, cm	Wavelength, cm
297	1500	4.5	9
300	1600	3	15
303	1300	3	8
307	1200	2–3	6–8

JD, Julian day.

During storm 2 the minimum in bottom position variability occurred at about JD 308.9 (Figure 10b), when the bottom shear stress approached and then exceeded the flat bed criterion (Figure 12b).

Throughout the remainder of the records, the times of larger-amplitude high-frequency bottom variability, the Shields parameter falls below the flat bed limit. Furthermore, comparing Figures 10 and 12, one sees that the larger rms amplitude variations in bottom distance coincide for the most part with those periods of time when the Shields parameter fell within the wave ripple existence region.

The reader will also note, however, that on two occasions large-amplitude variations are present even when the estimated values of the Shields parameter fall below the lower limit for ripple existence. These occur at the beginning of storms 1 and 2. In fact, however, we know from the acoustic backscatter measurements that considerable amounts of sediment were being lifted into suspension during these periods, so the threshold for grain motion was certainly being exceeded. We attribute this to three effects: the rippled state of the bed at the beginning of a storm; wave groupiness; and wave-current interaction. The lower limit for ripple existence is based upon the initiation of grain motion for an initially flat bed. In this experiment the bed was rippled at the beginning and end of each storm (as clearly shown by the

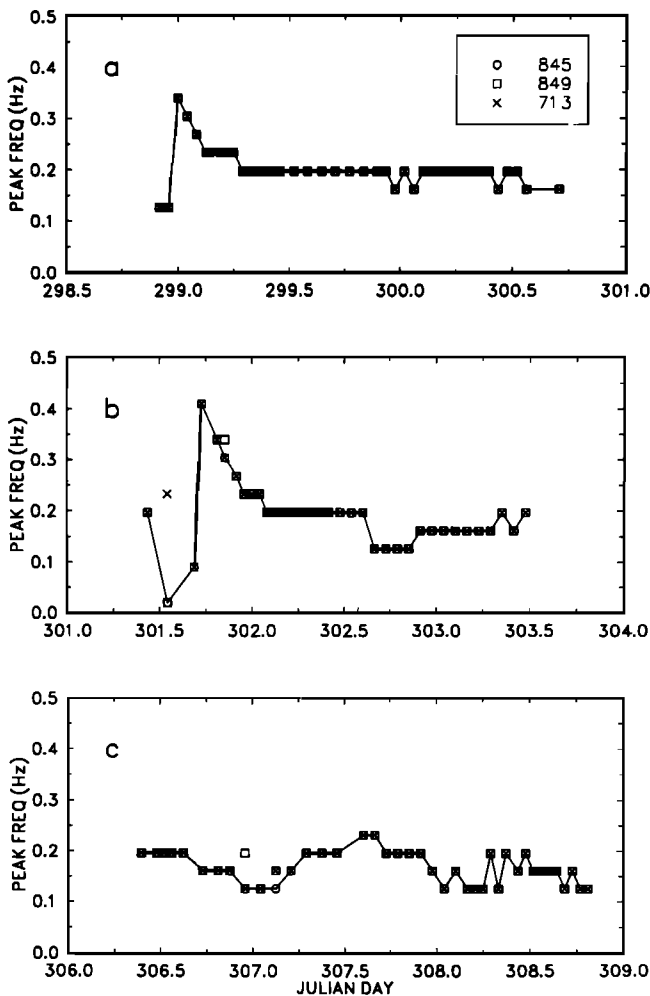


Fig. 11. Peak wave frequency ($1/T_p$) during (a) storm 1, (b) storm 2, and (c) storm 3.

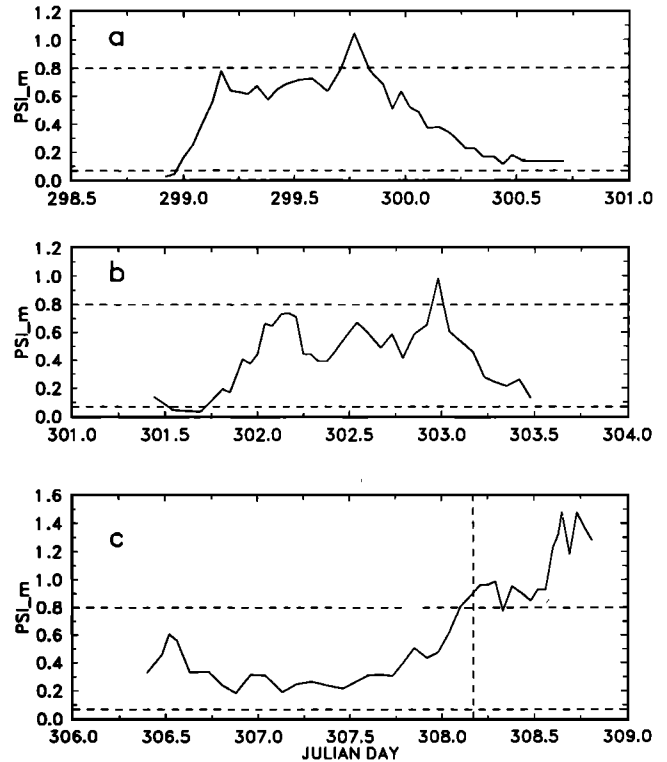


Fig. 12. Shields parameter during (a) storm 1, (b) storm 2, and (c) storm 3. The horizontal dashed lines indicate the upper and lower thresholds bounding the nominal wave ripple existence domain. The vertical dashed line in Figure 12c denotes the transition to flat bed on JD 308.17.

video camera), and was most unlikely to have been flat as the storms waxed and waned. As *Sleath* [1984, p. 144] points out, changes in the profile of an already rippled bed may take place at velocities much less than the critical velocity for grain motion. The second effect is that the Shields parameter estimates do not take wave groupiness into account. Estimates for the lower limit (the threshold of grain motion) based on the rms wave orbital velocity will necessarily be too high if the wave field is groupy. Finally, wave-current interaction, particularly with the longshore current early in the second storm (Figure 6c), may have been important. As emphasized in the work of *Grant and Madsen* [1979, 1986], the net effect is to produce a nonlinear increase in the bed shear stress partly through an increase in the apparent bed roughness. We have not taken wave-current interaction effects into account directly. The mean currents were usually much weaker than the wave velocities except at the beginning of storm 2 and at the end of the storm 3 record (when ripples were not present anyway), so it can be presumed that the ripples were wave-dominated [see *Sleath*, 1984, p. 168].

The rms amplitude of the high-frequency bottom distance variations therefore varies in a manner consistent with known wave ripple behavior: that is, rms amplitudes are large when the Shields parameter lies within the ripple existence domain, and amplitudes are much reduced at large values of the Shields parameter when flat (or nearly flat) bed conditions would be expected. This is the second point in our argument that the high-frequency variations are due to ripples.

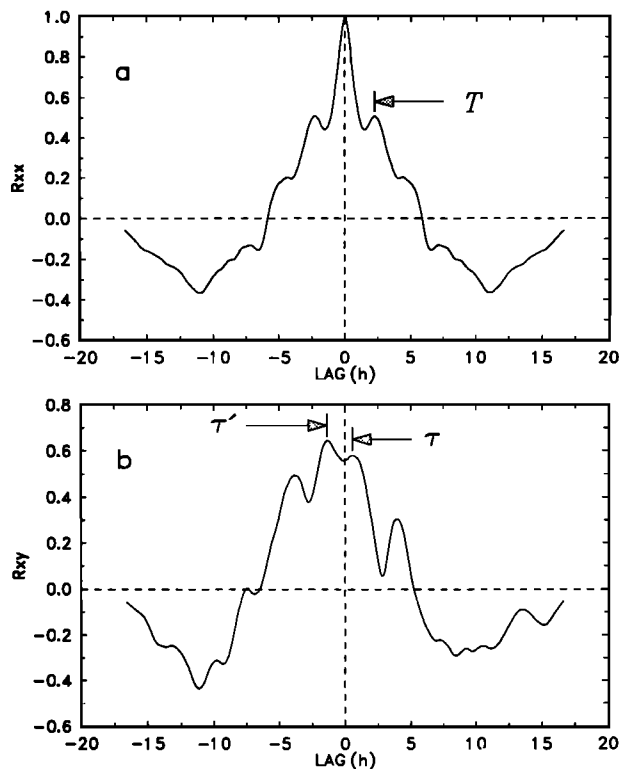


Fig. 13. (a) Example autocorrelation function from sounder 2C, and (b) cross-correlation function for sounders 2C and 1A (positive lag means 1A lags 2C), corresponding to the first time segment in storm 1. The symbols τ and T are defined in the text.

3.6. Ripple Wavelengths and Migration Velocities

Having demonstrated that the high-frequency variations can reasonably be attributed to sand ripples, we now proceed to extract estimates of ripple wavelength and migration velocity from the bed elevation time series obtained with the most closely spaced sounders. We restrict our attention to the onshore-offshore direction and for the moment to the data from sounders 2C and 1A, which were separated by 22 cm in the horizontal (Figure 2).

Figure 13 shows the lagged autocorrelation for sounder 2C, and cross-correlation functions for sounders 1A and 2C from the first storm. The autocorrelation function exhibits a long time-scale quasi-periodic signature, with period $O(20)$ hours (Figure 13a, with only the first three quarters of the cycle shown), corresponding to the low-frequency bottom elevation variations during this storm (Figure 3). Superimposed on this long period change is a high-frequency quasi-periodic signal, with period $O(3)$ hours. Similar behavior at high and low frequencies is present in the cross-correlation functions, as illustrated by the example in Figure 13b. This is the type of behavior expected of a spatially periodic wave train superimposed on a longer period undulation, propagating past a pair of spatially separated detectors: that is, sand ripples migrating on a slowly varying bed.

Suppose now that the ripples migrate at speed c , as sketched in Figure 14. Then the period T of the high-frequency signal in the autocorrelation function is given by

$$T = \lambda/c, \quad (3)$$

with λ being the ripple wavelength. If the sensor separation L were small (less than half a ripple wavelength), then the lag τ corresponding to the first high-frequency peak (the one at the shortest lag) in the cross-correlation function would yield the migration speed directly; that is,

$$c = L/\tau, \quad (4)$$

and the migration direction would be given by the sign of the lag. Furthermore, the ripple wavelength would be given simply in terms of known quantities by

$$\lambda = L/(\tau/T). \quad (5)$$

In our case, however, the sensor separation (22 cm) is comparable to or greater than the ripple wavelengths observed between storms (Table 2). Furthermore, previous work [Inman, 1957; Miller and Komar, 1980] would suggest that the ripple wavelengths should either have remained approximately constant or have decreased during the storms for the observed range of wave orbital diameters. The condition $L < \lambda/2$ is therefore not likely to have been satisfied. This leads to ambiguities in both wavelength and direction, as a result of spatial aliasing. Note that this is not a limitation of the method in principal and arises only because of our choice of sensor separation. The 22-cm separation was a compromise and involved a number of considerations, among these being the need to span the range of possible horizontal scales that might occur among the bedforms. Ripples were not the only bedform present, nor apparently were they the most important contributors to the apparent bedload transport, as will be seen. The larger separations (up to 1.5 m) between the three sounders along the length of the frame turn out to have been about right for these other bedforms.

It is possible to remove the aliasing effects from the measurement so that estimates of ripple properties can be made, as is shown below. Although the analysis is more complicated than it would have been otherwise, the additional complications seem to us to be warranted by the results. The principle assumption made is that the ripple wavelength spectrum is bounded from below, that is, that there is a minimum to the possible ripple wavelengths for the sediment size and wave orbital diameters at the RASTRAN location. Previous work [Inman, 1957; Miller and Komar, 1980] suggests that this should be the case for wave-generated vortex ripples. In the sense that we take advantage of an upper bound to the frequency spectrum to interpret aliased results, the analysis presented below is not without precedent in the literature. Large and Pond [1981, 1982], for example, exploited the fact that turbulence spectra

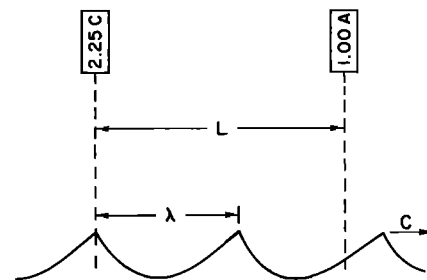


Fig. 14. Sketch showing spacing of sounders 2C and 1A relative to ripples.

TABLE 3. Ripple Wavelengths and Migration Velocities, with the Time Intervals in Each Storm Used in the Analysis, and the Corresponding Values of T and τ

Storm	Interval, JD	T , hours	τ , hours	τ' , hours	n	λ , cm	c , cm h ⁻¹	$\langle u \rangle$, cm s ⁻¹
1	298.837–300.583	3.26	1.30	-1.12	1	15.1 ± 1.4	-4.6	-3.0 ± 0.4 (1.9)
	298.837–299.601	2.25	0.54	-1.38	1	13.1 ± 0.6	-5.8	
	299.604–300.583	3.60	1.76	-0.94	1	16.0 ± 1.4	-4.4	
2	301.691–303.500	4.0	0.62	-2.9	1	12.4 ± 0.4	-3.1	-3.9 ± 0.8 (3.4)
3	306.396–308.354	8.0	0.30	-0.22	2	8.5 ± 1.0	-1.1	-1.6 ± 1.0 (2.4)
					1	14.1 ± 2.8	-1.8	

The error in λ is half the difference of the results for τ and τ' . Two error bounds are shown for $\langle u \rangle$: the first value is half the difference of the mean values from flow meters 845 and 849; the second value (in parentheses) is the root of the mean of the u variances for these two flow meters. JD, Julian day.

are bounded at high frequencies and set up a deliberately aliased sampling scheme to measure the Reynolds flux in the atmospheric boundary layer over the ocean.

Suppose we have two periodic signals, $r_1 = r_0 \cos \omega t$ and $r_2 = r_0 \cos (kL - \omega t)$, where $\omega = 2\pi/T$ is the angular frequency, and $k = 2\pi/\lambda$ is the wavenumber. The direction of propagation is positive (shoreward). The separation is such that $n\lambda < L < (n + 1)\lambda$, n a positive integer (Figure 14). The cross-correlation function constructed from two such signals will have a first maximum at positive lags (r_1 leads r_2) given by

$$\tau/T = L/\lambda - n, \quad \tau > 0, \tag{6}$$

and a first maximum at negative lags given by

$$\tau'/T = L/\lambda - (n + 1), \quad \tau' \leq 0. \tag{7}$$

It is not known immediately which of the two lags, the negative or the positive one, represents the actual direction of propagation. This is the directional ambiguity. These equations also illustrate the wavelength ambiguity. Rearranging, one obtains

$$\lambda = L/(n + \tau/T), \quad \tau > 0, \tag{8}$$

$$\lambda = L/(n + 1 + \tau'/T), \quad \tau' \leq 0. \tag{9}$$

It is clear comparing (6)–(9) with (5) that if one were to use either τ or τ' to compute λ from (5), the values of λ so obtained would be too large. The wavelength ambiguity, if left uncorrected, therefore causes the expected shift of information from high (spatial) frequencies to low (spatial) frequencies, due to the aliased spatial sampling scheme (Figure 14).

For propagation in the negative direction, $r_2 = r_0 \cos (kL + \omega t)$, these relationships become

$$\lambda = L/(n - \tau/T), \quad \tau < 0, \tag{10}$$

$$\lambda = L/(n + 1 - \tau'/T), \quad \tau' > 0. \tag{11}$$

Values of T , τ , and τ' were determined for all three storms and are listed in Table 3. Storm 1 was chosen as a test case and was separated into two time segments because the diver measurements indicated that an increase in ripple wavelength occurred as a result of the storm (Table 2). It was found that in order to produce an increase in wavelength over the two time segments, seaward propagation of the ripples had to be assumed. (Shoreward phase propagation resulted in a decrease in wavelength.) The wavelengths for

storm 1, estimated assuming $n = 1$ and averaging the results for τ and τ' , are listed in Table 3. They are all about 15 cm, similar to the diver measurement made after the storm, and show a slight increase (from 13 to 16 cm) between time segments, as required. The fact that this increase is not as great as that observed may be attributed to the correlation estimates representing an average over a relatively long time, $O(1 \text{ day})$, the length of the time segments.

The wavelengths computed for the other two storms assuming seaward propagation are also listed in Table 3. The wavelength estimate for storm 2 (12 cm, $n = 1$), is seen to be less than those for storm 1, also as was observed by the divers. (Assuming shoreward phase propagation produces the reverse result.) Again, the fact that this estimate is longer than the diver-observed value after the storm (8 cm), but about equal to the average of the before and after diver values (11.5 cm), can reasonably be attributed to the correlation result representing an average value for the storm. The best wavelength estimate for the third storm is at that point taken to be that made with $n = 2$ (8.5 cm), which is consistent with the diver measurements. Even so this value is a bit large. (Shoreward phase propagation yields a still larger value, 9.5 cm).

We suggest on the basis of this analysis that the ripples were migrating offshore on average during storms 1 and 2, and the first part of storm 3 (prior to the flat bed transition). This conclusion is supported by the current measurements which registered a mean seaward drift during each storm (Figures 4, 6, and 8). (Note with respect to storm 3 that the analysis was carried out only for the period preceding the transition to the flat bed on JD 308.17. During this period the mean drift was seaward (Figure 8). Other work has also shown that in combined flows, wave ripples migrate in the direction of the mean current [Dingler and Inman, 1977; Amos et al., 1988].

It is also interesting to point out that seaward ripple migration is consistent with Dean's [1973] direction index for onshore-offshore sediment transport. As taken from Sleath [1984, p. 299], this parameter is

$$\Gamma = 0.6h_0gT_p/\pi\lambda'_0W_s, \tag{12}$$

where h_0 and λ'_0 are the wave height and length in deep water, and W_s is the settling velocity. Using the deep water dispersion relation from linear wave theory to substitute for λ'_0 , Dean's parameter becomes $1.2h_0/W_sT_p$. This form illustrates the physical basis of the parameter, which is a measure of whether or not sediment lifted into suspension under a wave crest will, on average, settle out during the first

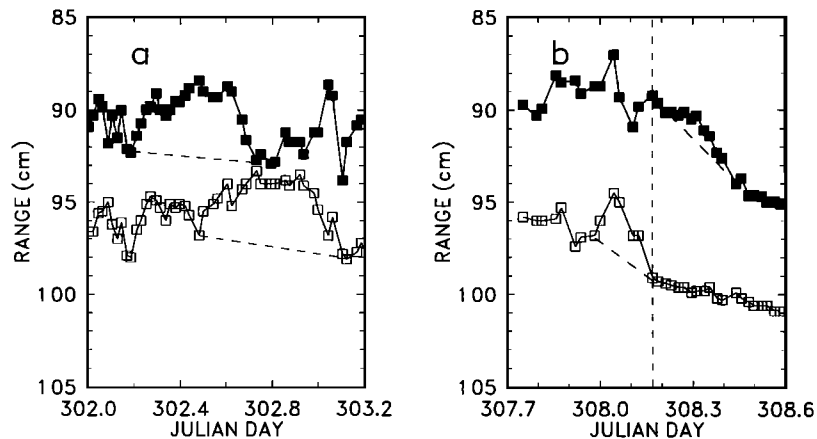


Fig. 15. Bed elevation time segments for sounder 2C (on the seaward end of the RASTRAN frame) and sounder 2D (landward end), showing migrating large-scale bedforms (megaripples), for (a) storm 2 and (b) Storm 3. The megaripples are indicated by the slanting dashed lines. The vertical dashed line in Figure 15b denotes the transition to flat bed on JD 308.17.

half cycle (shoreward transport and small Γ), or during the last half cycle (seaward transport and large Γ). As such, the parameter should be relevant to the probable direction of ripple migration. For 170- μm -diameter quartz sand, the settling velocity is nominally 2 cm s^{-1} . For the wave periods encountered here, $\Gamma = 7\text{--}12h_0$, so $\Gamma \gg 1$ for any reasonable choice of offshore wave height during these storms, implying seaward transport.

Ripple migration speeds, computed using (3), are also listed in Table 3. They are in the range $1\text{--}6 \text{ cm h}^{-1}$, decreasing from storm 1 to storm 3, for mean offshore drift speeds in the range $2\text{--}4 \text{ cm s}^{-1}$ (Table 3). Within the uncertainty of the mean offshore drift estimates, the migration speeds tend to increase with increasing mean current speed. These migration rates are within the range of values obtained in other field measurements. In the only other measurements from the nearshore zone of which we are aware, *Dingler and Inman* [1977] obtained values ranging from 0 to 250 cm h^{-1} , which also increased with increasing mean current speed. For (estimated) mean currents of about 3 cm s^{-1} , however, their data suggest migration rates of $30\text{--}60 \text{ cm h}^{-1}$, significantly larger than those found here and in other studies. For example, *Amos et al.* [1987] measured values between 0.4 and 4 cm h^{-1} for wave-generated ripples in mean current ranging up to 40 cm s^{-1} on the Scotian shelf near Sable Island in 20 m water depth. (At this depth the seabed was influenced by both surface waves and tidal currents.) In a tidal channel experiment with no wave influence reported, *Sternberg* [1967] found average migration rates for current ripples of about 10 cm h^{-1} in mean currents of 25 cm s^{-1} (measured 10 cm above the bed). The migration rate varied with mean speed approximately to the fifth power, consistent with laboratory results. *Dyer and Soulsby* [1988] reported (current) ripple migration speeds in the range $1.2\text{--}120 \text{ cm h}^{-1}$ (which also increased with increasing current speed but to nothing like the fifth power) in tidal currents of $20\text{--}60 \text{ cm s}^{-1}$.

Other field studies of ripple migration rates, therefore, though few in number, tend to support the present results at least in terms of migration direction relative to that of the mean drift. Our estimates of migration speeds also appear to be reasonable, although they are lower by an order of magnitude than those obtained by *Dingler and Inman* [1977]

under what would at first appear to be comparable mean flow conditions. However, the mean flows reported by *Dingler and Inman* are theoretical estimates of the mean wave-induced bottom drift, rather than actual measurements. This may account for much of the difference in the observed migration rates. In addition, our estimates represent average values for each storm, whereas those of *Dingler and Inman* are based on bed profile measurements made minutes apart.

3.7. Megaripples

Large-scale bedforms (megaripples) have been observed in the nearshore zone, in both barred [*Davidson-Arnott and Greenwood*, 1976; *Hunter et al.*, 1979; *Greenwood and Mittler*, 1979; E. B. Thornton, personal communication, 1991], and unbarred [*Clifton et al.*, 1971] systems. These megaripples have usually been characterized as being lunate in shape, with wavelengths (distances between troughs) of order 0.5 to 5 m. During storm 2, a 90° phase difference occurred between sediment accumulation at either end of the frame (Figure 5c). This can be interpreted as being due to the seaward migration of a large-scale bedform. That is, the 3-cm amplitude maximum in seabed elevation observed at the landward end of the frame on JD 302.5 is the crest of a megaripple which migrated to the offshore end by JD 302.8. The migrating megaripple is seen more clearly in Figure 15a, which shows, on an expanded time scale, a subset of the bottom distance data from the two 2.25-MHz sounders at opposite ends of the frame. The megaripple profile in Figure 15a is very similar to the profiles given by *Clifton et al.*: a broad crest of nearly uniform height bounded front and rear by much sharper troughs. A mean translation time of $0.3\text{--}0.4$ day for the feature is obtained from Figure 15a. This translation time and the 1.45-m separation of the sounders give a phase speed of $15\text{--}20 \text{ cm h}^{-1}$. The time between consecutive seabed elevation minima at either sounder is about 0.6 day. Combining this observed period with the phase speed gives a wavelength λ of $2.2\text{--}2.9$ m.

The possible observation of a large-scale bedform was also discussed previously in relation to the storm 3 record, during the latter part of which (after flat bed transition and before general local erosion) the response of the bed at the shoreward end of the frame exhibited a pronounced lag compared

to that at the seaward end. Examining Figure 15*b*, a detail from Figure 7*a*, one can argue that the maximum in bed elevation at the seaward end of the frame on JD 308.05 was the crest of a megaripple which subsequently migrated shoreward to reach the landward end at about JD 308.3 (Note that landward migration at this point in storm 3 does not contradict our conclusion that the ripple transport was seaward earlier in this storm. In fact, the entire bar moved shoreward during the latter part of storm 3, as was documented independently by the diver observations on JD 307 and JD 310, so that the inferred migration direction for this megaripple is consistent with the shoreward migration of the bar. Furthermore, shoreward migration is also consistent with the reversal of the measured near-bottom shore normal drift from offshore to onshore during this period. See Figure 8*d*). The 0.25-day translation time gives a phase speed of 24 cm h⁻¹. The time between consecutive bed elevation minima bracketing the bed elevation maximum is about 0.24 day, which gives a wavelength of 1.4 m. This phase speed and wavelength are comparable to the values for the storm 2 megaripple.

4. DISCUSSION

4.1. Ripple Migration Versus Ripple Eradication

Dingler [1974] found that ripples could be obliterated by large waves during the passage of wave groups, resulting in a flat bed. Ripples were then reconstructed by the smaller waves between groups. This eradication/reconstruction sequence would produce high-frequency fluctuations in bottom elevation similar to those in Figure 10 and therefore might provide an alternative to the ripple migration mechanism. The available evidence from the Stanhope '89 experiment indicates, however, that ripple eradication on time scales of a few wave cycles as observed by Dingler did not occur. The evidence comes directly from the acoustic backscatter measurements and is supported by the video camera observations.

The video camera was monitored continuously during each storm, using underwater lights at night and ambient light during the day, and was recorded on VHS format video tape on a regular basis. During active suspension events, the bottom was obscured from view as was mentioned previously. Nevertheless, it was often possible to observe the undulation of the sediment cloud as it moved back and forth over the underlying ripples during the passage of wave groups. The bed was never seen to go flat during the passage of a group. Instead, the ripple field emerged essentially unaltered, in terms of the ripple pattern at least, after the sediment cloud had dissipated.

The acoustic backscatter profiles were acquired at a rate of 6.6 Hz during 6.5-min runs [Hay and Sheng, 1992]. Typically four 6.5-min runs were made for every half hour UDATS run. The vertical resolution of the stored backscatter profiles was 1.8 cm. Although this resolution is coarser than the ± 1 mm resolution of the bottom elevation measurements presented here, changes in bottom elevation of ± 1 –2 cm would produce a range bin shift in the position of the bottom echo. This means that if the ripples, which had heights of 3–5 cm, were obliterated by a wave group, then changes in the position of the bottom echo would have been recorded in the backscatter profiles for the different sound-

ers. Such changes were observed, but infrequently (typically less than once per 6.5-min run).

Both the video observations and the acoustic backscatter time series indicate a comparatively slow evolution of the bed, on time scales of many minutes rather than a few wave periods, consistent with the migration of ripples at speeds of several centimeters per hour. As was mentioned above, this differs from Dingler's [1974] observations of transition from a rippled to a flat bed produced by a single wave group, and of ripple migration rates of up to several meters per hour. Some possible reasons for the higher migration speeds have been pointed out already. The two pictures, one of a slowly evolving ripple field and the other of a rapidly changing bed alternating from flat to rippled between wave groups, are nonetheless very different and need to be reconciled. We expect that both pictures are probably correct, and represent two end-members of a continuum which depends upon wave conditions and location relative to the surf zone. The constraints for the two experiments were different. The main site selection criterion used by Dingler was "to have a wave environment with sufficient energy to produce sheet flow-conditions at the bed" [Dingler, 1974, p. 55]. This was not a criterion for choosing the RASTRAN location and suggests that location with respect to the surf zone may account for some of the differences in the observations. Dingler's observations were made on the Pacific coast of North America, where wave periods are typically longer than on the Atlantic coast. The period of the waves which produced flat bed in the example given by Dingler [1974, Figure 24] was 9 s, compared to the 5–6 s typical of our measurements. It appears to be easier to eradicate ripples with longer-period waves. However, although orbital velocities tend to be larger for the longer-period waves, particularly those associated with groups, the differences are not very great. Eradication may be related to the persistence of higher velocities during longer-period waves.

4.2. Ripple Properties

We now compare our measurements of ripple wavelength and height with the known properties of wave-formed ripples. This provides a further consistency test for the amplitude and migration rate results obtained in a previous section.

The wavelength results are compared in Figure 16 with the known behavior of wave-formed ripples as a function of wave orbital diameter and grain size, as compiled by Miller and Komar [1980]. The data from the present study are shown as the mean ripple lengths for each storm plotted against the significant wave orbital diameter $2\langle u_{\text{rms}} T_p \rangle / \pi$ (angle brackets denote the average over the storm), computed for one of the near-bottom flow meters (845, Figure 2). (Points are plotted for both time segments of storm 1, for storm 2, and for both $n = 1$ and 2 for storm 3.) One sees that within the scatter of the data, our derived wavelengths generally lie in the region of the diagram expected for wave ripples in 170- μm -diameter sand. A possible exception is the $n = 2$ point for storm 3, for which the wavelength appears to be too short. Consistency with previous results is improved by taking the $n = 1$ estimate.

Ripple steepness η/λ , where η is the ripple height, can be compared with the results of previous work using Nielsen's [1981] empirical formula for wave-generated ripples:

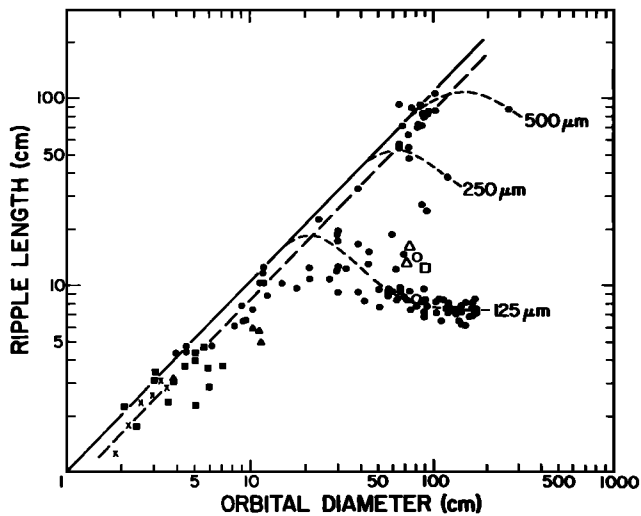


Fig. 16. Ripple wavelength estimates obtained from the lagged correlation analysis plotted against significant wave orbital diameter and superimposed on previous wave ripple data (solid circles and crosses) as compiled by Miller and Komar [1980]. Symbols represent data points for the different storms: storm 1, time segments 1 and 2 (open triangles); storm 2 (open squares); and storm 3, $n = 1$ and 2 (open circles).

$$\eta/\lambda = 0.342 - 0.34\sqrt[4]{\psi}. \quad (13)$$

This formula is based on field measurements made by Inman [1957] and Dingler [1974]. Mean ripple steepnesses were computed for each storm from the time series of ψ estimates (Figure 12) and are listed in Table 4 as $\langle\eta/\lambda\rangle$, where angle brackets again denote the average over the duration of the storm (for storm 3, up to the flat bed transition). For comparison, estimates of mean ripple height η_{rms} were computed from the high-frequency variations in bottom position (Figure 10) such that η_{rms} is $2\sqrt{2}$ times the square root of the variance. This was done for each of the sounders in the three-frequency cluster. The values listed are the three-sounder averages. The measured ripple steepness is therefore η_{rms}/λ , taking λ from Table 3, and necessarily assumed to be constant throughout each storm. The agreement between the measured ripple steepnesses for the first two storms and the values given by (13) is acceptable. For the third storm, however, the $n = 2$ estimate is larger than the result of (13) by more than a factor of 2. Choosing the $n = 1$ value reduces η_{rms}/λ to a value more consistent with (13), again suggesting that the mean wavelength for this storm is underestimated by taking $n = 2$.

Both comparisons above indicate that it may have been inappropriate to force agreement with the diver measurement made on JD 307 during a lull in storm 3 by setting $n = 2$ and that the $n = 1$ wavelength and phase speed are more representative of the mean ripple properties for this storm.

4.3. Megaripple Properties

The large-scale bedforms are similar to those of megaripples that have been observed in the nearshore zone by others, in terms of their location relative to the beach profile, their geometric properties, and their migration velocities. Clifton *et al.* [1971] found lunate megaripples immediately seaward of the surf zone on an unbarred beach. On barred beaches, lunate megaripples have been observed on and immediately seaward of the submerged bar crest on crescentic bars [Davidson-Arnott and Greenwood, 1976], oblique bars [Hunter *et al.*, 1979], and straight bars [Greenwood and Mittler, 1979]. E. B. Thornton (personal communication, 1991) has also observed megaripples on the seaward face of a straight bar. It is interesting to note that Clifton *et al.* report a 30 cm h^{-1} migration rate for their megaripples, which is comparable to our $15\text{--}25 \text{ cm h}^{-1}$ estimates. Both seaward and landward migration directions have been inferred from sediment texture analysis [Clifton *et al.*, 1971; Davidson-Arnott and Greenwood, 1976; Greenwood and Mittler, 1979]. The similarity of the megaripple profiles indicated by Figure 15 to those given by Clifton *et al.* has been mentioned. Clifton *et al.* give values of 30–100 cm for height, and 0.5 to 5 m for length (distance between troughs). Thornton found heights up to 30 cm and lengths up to 10 m. The lengths of the features in Figure 15 are 1.5–3 m, well within the megaripple range. The heights are 2–5 cm, small in comparison with these other studies. However, Clifton *et al.* found that megaripple size can vary significantly with wave period and wave height. The 50- to 100-cm megaripple heights cited above are for the 10- to 14-s period, 1.5- to 2-m (highest tenth) waves typical of conditions during their study on the Oregon coast. Under shorter-period (6 s), lower-amplitude (0.8 m highest tenth) waves, they observed that the megaripples became irregular, losing their lunate shape, and more difficult to recognize. This suggests that the small heights found here are at least partly due to the waves being of shorter period (6–8 s) than is typical off Oregon.

4.4. Bedload Transport Rates

Bedform migration rates can be used to estimate the bedload transport Q_b in unidirectional oceanic flows (see, for

TABLE 4. Ripple Heights and Steepnesses, Ripple Transport Rates, and Measured Suspended Sediment Transports Associated With the Storm-Mean Shore Normal Drift (u) (Table 3)

Storm	η_{rms} , cm	n	η_{rms}/λ	$\langle\eta/\lambda\rangle$	$\rho_0 Q_s$, $\text{g cm}^{-1} \text{h}^{-1}$	$\langle\bar{M}\rangle$, g L^{-1}	$\rho_0 q_s$, $\text{g cm}^{-1} \text{h}^{-1}$
1	2.0 ± 0.3	1	0.13	0.076	-10.	0.128	-68
2	2.3 ± 0.4	1	0.18	0.075	-8.3	0.159	-110
3	2.5 ± 0.3	2	0.30		-3.1		
		1	0.18	0.077	-5.4	0.117	-34

\bar{M} is the suspended sediment concentration obtained from the three frequency acoustic backscatter amplitudes [Hay and Sheng, 1992], vertically averaged from 1 to 50 cm height above bottom (i.e., $\Delta h = 49 \text{ cm}$).

TABLE 5. Bedload Transport Rates Predicted by the MG [Madsen and Grant, 1977] and WVS [Watanabe, 1981; Vincent et al., 1981; Sleath, 1982] Formulae

Storm	$\rho'_0 \langle Q_s \rangle$, g cm ⁻¹ h ⁻¹	
	MG	WVS
1	720 ± 910	620 ± 510
2	610 ± 750	590 ± 440
3	450 ± 720	480 ± 400

The error bounds represent ± the square root of the variance.

example, McLean [1983] and Dyer and Soulsby [1988]), the transport being given by the product of the bedform volume and its migration speed. We shall assume that a similar calculation for migrating ripples in combined flows also yields an estimate of the bedload transport.

Assuming a sinusoidal ripple profile, the mass transport rate per unit length of a straight-crested ripple is given by

$$\rho'_0 Q_s = 0.66 \rho'_0 (1 - \phi) \eta_{rms} c, \quad (14)$$

where ρ'_0 is the sediment grain density (2.7 g cm⁻³ for quartz sand) and ϕ is the porosity of the sediments (0.35 for medium to fine sand [Sleath, 1984, p. 120]). Substituting these values, and the values of η_{rms} and c from Tables 3 and 4, one obtains the ripple mass transport (Table 4).

The transport values listed in Table 4 indicate that ripple transport does not appear to have represented an important component of the local sediment budget on the middle bar during these storms. As one measure of this, we may compare the ripple transport rate with the mass transport of suspended sediment due to the mean offshore drift. A rough estimate of this transport is given by

$$\rho'_0 q_s = \langle \bar{M} \rangle \langle u \rangle \Delta h, \quad (15)$$

where \bar{M} denotes the vertical average of M , the mass concentration of suspended sediment, over a column of height Δh above the bottom. The three-frequency acoustic backscatter profiles can be processed to obtain vertical profiles of suspended sediment concentration and size. This problem is treated elsewhere [Hay and Sheng, 1992]. For the purposes of the present article, the resulting concentration profiles have been vertically averaged over the height interval 1–50 cm and time averaged over the duration of each storm to obtain $\langle \bar{M} \rangle$. These values are listed in Table 4 and are of the order 100 mg L⁻¹. (Note that such values are typical of results that have been obtained with single-frequency acoustic backscatter profilers in the nearshore zone [e.g., Hanes et al., 1988; Vincent et al., 1991].) The values listed in Table 4 for the suspended sediment transport due to the mean offshore drift alone are an order of magnitude greater than the seaward ripple transports.

The estimates of bedload transport by ripples can also be compared to existing semi-empirical formulae for bedload transport under waves. Two commonly used formulae, both based upon laboratory measurements, are

$$Q_s = 12.5 W_s D \psi^3, \quad (16)$$

from Madsen and Grant [1977], hereinafter denoted MG, and

$$Q_s = 7 W_s D (\psi - \psi_c) \psi^{1/2}, \quad (17)$$

from Watanabe [1981], Vincent et al. [1981], and Sleath [1982], denoted WVS. The WVS formula explicitly includes ψ_c , the critical Shields parameter for initiation of movement, which is taken to be 0.07 here (Figure 12). The constant factor 7 is from Watanabe [1982] and is based on measurements made in regular waves. (We note in passing that values of 1–3 for this factor have been found to give better agreement for measurements made with irregular waves [Mimura et al., 1987; Horikawa, 1988, p. 209; Kraus and Horikawa, 1990].) The storm mean values $\rho'_0 \langle Q_s \rangle$ computed using each of these formulae are listed in Table 5. The two formulae yield very similar results, with the WVS values being somewhat smaller, as expected for the ψ range encountered here [Horikawa, 1988, p. 207].

The MG and WVS bedload transports exhibit roughly the same trend as the ripple transports in Table 4, decreasing from storm 1 to storm 3, but are nearly 2 orders of magnitude larger. One might justifiably increase the ripple transport values by a factor of 2 by doubling the ripple heights. This would amount to using the significant ripple height instead of the mean ripple height but would still not account for the discrepancy, and our choice of a sinusoidal ripple profile probably overestimates the ripple volume in any case. One might also attribute the discrepancy to the ripple transports being minimum estimates because of the use of a storm mean migration rate. (As one way of testing this, we determined the inverse effect by computing the mean bedload transport using the above formulae and the storm mean Shields parameter $\langle \psi \rangle$. This reduces the MG estimates by more than a factor of 2 but reduces the WVS estimates by only 10%.) One might also invoke the uncertain accuracy of the bedload formulae [e.g., Sleath, 1984, p. 265]. Another possibility, however, is that the ripple transport accounts for only part of the total bedload.

Estimates of megaripple migration rates were made in the previous section. Substituting the height (3 cm) and phase speeds (15–20 cm h⁻¹) for the storm 2 megaripple into (15) gives $\rho'_0 Q_s = 50$ –70 g cm⁻¹ h⁻¹ for the transport rate. For the storm 3 megaripple (2–3 cm height, 24 cm h⁻¹ phase speed) a transport rate $\rho'_0 Q_s = 56$ –84 g cm⁻¹ h⁻¹ is obtained. These large-scale bedform transport rates are an order of magnitude greater than the ripple transports, illustrating the point that the ripple transport need not necessarily represent the total bedload. Nevertheless, the total bedform transport rate (ripple plus megaripple) is still only about 10% of the values predicted by (16) and (17). The bedform transport rates could be made larger by using a more realistic (nonsinusoidal) megaripple profile. However, dramatically improved agreement with the WVS formula, to within a factor of 2 or better, would be obtained by using the $O(1)$ values for the constant factor (instead of the value 7), as suggested by the laboratory measurements made with irregular waves.

Summarizing, the preceding calculations indicate that the ripple transport rate was small. In contrast, that component of the bedload transport associated with the larger-scale bedforms (megaripples) appears to have been potentially an order of magnitude larger than the ripple transport and thus comparable to the mean drift of suspended sediment normal to the shoreline. The comparisons between the total bedform transport rates and those predicted by the WVS net bedload

transport formula are improved if a value of $O(1)$ is taken for the constant multiplicative factor, as has been suggested for irregular waves [Mimura *et al.*, 1987; Horikawa, 1988].

The onshore migration of the bar during the latter part of storm 3 raises several issues which at this point we mention but leave unresolved. Neither bedload formula predicts onshore migration of the megaripple and the bar, illustrating one of the outstanding problems with bedload transport estimation in the nearshore: determining the net transport direction [Kraus and Horikawa, 1990]. Nor does Dean's [1973] criterion predict onshore migration, at least as long as one assumes constant and uniform size for the bottom sediments. The possible ramifications of this not being a valid assumption have been considered for some time in relation, for example, to the null-point hypothesis, equilibrium beach profiles, and the process of bar formation [e.g., Bowen, 1980] and highlight the potential importance with regard to morphological change of measuring sediment size during the course of a storm. We point out as well that the onshore migration of the bar as the waves were growing is contrary to conventional wisdom, which would predict that the opposite should occur. Yet this phenomenon has been observed at Stanhope Beach three times: first in 1985 during the Canadian Coastal Sediment Study [Hanes *et al.*, 1988], then during a storm that occurred while we were deploying our instrumentation in 1989, and again during storm 3. Onshore migration during storm 3 was consistent with the observed weakening of the undertow, however, indicating that any plausible explanation may well have to incorporate the dynamics of the shorenormal flow.

No obvious large scale bedform was observed during storm 1 or the first part of storm 3. The discrepancy between the total bedform transport rate and the WVS prediction with coefficient $O(1)$ therefore remains for these periods and requires explanation. We suggest that the discrepancy may only be apparent and that it reflects mainly the limited spatial coverage of our measurements. For example, given the three-dimensional character and irregular spatial separations of the megaripples observed by Clifton *et al.* [1971], it would be possible for the telltale troughs of a 5-m-long ripple migrating at 20 m h^{-1} to remain undetected by the echosounder beams for times at least as long as 25 hours. This could explain their apparent absence during storm 1 and the first part of storm 3. Furthermore, it is clear given the limited observations that we know little about the development of megaripples and other large-scale bedforms during storms: the observation by Clifton *et al.* relating megaripple variability to wave period and height is clearly important and needs to be pursued. This will require systems capable of providing more extensive bottom coverage. Such developments are in progress.

We have defined the bedload transport rate in terms of a measureable quantity: the bedform transport rate. This operational definition has practical advantages. However, the sediments participating in the migration of the bedform are at times lifted well above the bed, where they will be detected by acoustic backscatter sensors. It then becomes less clear as to how to properly compare "suspended" sediment transport rates based on concentration profile measurements with "bedload" transport rates based on bedform migration. Sleath [1984, p. 309] also raises this issue and, for combined flows over rippled beds, includes the plumes of sediment lifted to several ripple heights above bottom in the bedload.

Such plumes would have been incorporated in our suspended load values. The processes of bedform migration and suspended sediment transport therefore cannot be entirely separated, unless one or the other can be assumed to be dominant. The estimates presented here indicate that this assumption is not always valid: that is, in the onshore-offshore direction the apparent suspended sediment transport rate (or, more precisely, that component of the suspended sediment transport associated with the mean shore normal drift) can be of the same order as the apparent bedform transport rate. The fact that the ripple and megaripple estimates do not agree suggests that suspension has to play a role.

5. CONCLUSIONS

We conclude that it is possible to determine the vertical position of a sand seabed in the nearshore zone under storm conditions to within a few millimeters using megahertz-frequency acoustic sounders mounted at a nominal height of 1 m above the bed. By making these measurements at several horizontally separated positions ranging from $O(10 \text{ cm})$ to $O(1 \text{ m})$, it is possible, through an examination of the space-time coherence of the bed elevations in relation to concurrent measurements of the fluid forcing, to estimate a range of seabed properties important to nearshore sediment transport. These are (1) the local bottom slope, (2) local erosion and deposition rates, (3) average sand ripple properties, including wavelength, height, and migration rate, (4) large-scale bedform properties, including length, height, and migration rate, and (5) transition to flat bed. Furthermore, the bedform information can be used to define the quantity which we have referred to as the bedform transport rate.

Ripple heights ranged from 3 to 5 cm peak (2–2.5 cm rms). Our best estimates of mean wavelengths range from 12 to 16 cm depending on the storm. These wavelengths are in the range expected for wave-generated ripples for the range of storm-mean significant wave orbital diameters (70–90 cm) encountered at the RASTRAN location during the Stanhope '89 experiment. The rms ripple heights and mean wavelength estimates give ripple steepnesses of about 0.1–0.2, consistent with Nielsen's [1981] empirical relation for wave-generated ripples, within the limits of accuracy of the measurements. The ripples migrated offshore, in the direction of the mean near-bottom shore normal drift, at rates of $3\text{--}6 \text{ cm h}^{-1}$. The migration rates tended to increase with increasing storm mean drift speed, which ranged from 1.5 to 4 cm s^{-1} .

On two occasions, megaripple-like features were observed to migrate through the array, with heights of 3–5 cm and lengths of 1.5–3 m. The migration rates in both cases were about 20 cm h^{-1} , directed offshore in one case and onshore in the other. In both cases these large-scale bedforms migrated in the direction of the mean shore normal near-bottom current.

Transition to flat bed was observed in the latter part of the third storm, coincident with a rapid increase in the wave Shields parameter and growth of the longshore current. Subsequently, we measured 12 cm of generalized local erosion beneath the RASTRAN frame over a period of several hours. The maximum observed erosion rate was 8 cm h^{-1} . This erosion event apparently occurred in response to further observed increases in the wave forcing and in the

strength of the longshore current and was associated with onshore migration of the bar. Such events have obvious importance for nearshore sediment dynamics but have rarely if ever been documented before.

The bedform results provide interesting insight into the direction and magnitude of the bedload transport. Such measurements open the possibility of estimating the relative importance of bedload and suspended load transport and of verifying the appropriate coefficients for bedload formulae when applied to irregular wave conditions. For example, our results for onshore-offshore transport indicate that in comparison to the shore normal suspended sediment transport associated with the mean shore normal drift, the ripple component of the bedload transport is small. The megaripple component of the bedload, on the other hand, may have been comparable to the mean drift in suspension. In addition, the values for total bedform (ripple plus megaripple) transport are comparable to the values predicted by the WVS bedload formula for irregular waves, with a coefficient of $O(1)$. These results are at best suggestive, however, as the appropriate coefficient in the WVS formula is not well established, and the need for more extensive observations to improve the statistics of the large-scale bedform transport estimates is clearly indicated. Nevertheless, the use of bedform migration rates to estimate bedload transport in the nearshore zone seems worth pursuing. The use of acoustic methods for this purpose is clearly promising, and the development of systems capable of providing more complete information on the bedform field is needed. In particular, the present results emphasize the requirement for three-dimensional bathymetric measurements over scales of $O(10$ m), so that the transport processes related to megaripple migration can be properly resolved.

Acknowledgments. We thank Eugene Colbourne and Jinyu Sheng for their assistance with the acoustic measurements, and David Hazen and Scott MacLean for their help with the hydrodynamic measurements. Many others are thanked for their assistance during the Stanhope '89 experiment: Brian Greenwood and the University of Toronto group, Rob Brander, Phil Osborne, and Ray Richards; Rick Dittman and Jack Foley from Memorial; and Chris Vincent and Andrew Downing from the University of East Anglia. We thank Ed Thornton for describing his megaripple measurements and for directing us to other megaripple observations in the literature. This study was funded by a Strategic Grant from the Natural Sciences and Engineering Research Council of Canada, and is part of the Canadian Coastal Sediment Transport (C-COAST) program.

REFERENCES

- Allen, J. R. L., *Sedimentary Structures: Their Character and Physical Basis*, vol. 2, 663 pp., Elsevier, New York, 1982.
- Amos, C. L., A. J. Bowen, D. A. Huntley, and J. T. Judge, Bedform stability under waves and currents, in *Proceedings of Workshop on Roughness and Friction, Rep. NRCC-29034*, pp. 62-74, Natl. Res. Council of Can. Assoc. Comm. on Shorelines, 1987.
- Amos, C. L., A. J. Bowen, D. A. Huntley, and C. F. M. Lewis, Ripple generation under the combined influence of waves and currents on the Canadian continental shelf, *Cont. Shelf Res.*, **8**, 1129-1153, 1988.
- Bowen, A. J., Simple models of nearshore sedimentation: Beach profiles and nearshore bars, in *The Coastline of Canada*, edited by S. B. McCann, *Pap. Geol. Surv. Can.*, **80-110**, 1-11, 1980.
- Clifton, H. E., R. E. Hunter, and R. L. Phillips, Depositional structures and processes in the non-barred high-energy nearshore, *J. Sediment. Petrol.*, **41**, 651-670, 1971.
- Davidson-Arnott, R. G. D., and B. Greenwood, Facies relationships on a barred coast, Kouchibouguac Bay, New Brunswick, Canada, in *Beach and Nearshore Sedimentation*, edited by R. A. Davis, Jr., and R. L. Ethington, *Spec. Publ. Soc. Econ. Paleontol. Mineral.*, **24**, 149-168, 1976.
- Dean, R. G., Heuristic models of sand transport in the surf zone, in *Conference on Engineering Dynamics in the Coastal Zone*, pp. 208-214, Institution of Civil Engineers, Sydney, Australia, 1973.
- Dingler, J. R., Wave-formed ripples in nearshore sands, Ph.D. thesis, 133 pp., Univ. of Calif., San Diego, 1974.
- Dingler, J. R., and D. L. Inman, Wave-formed ripples in nearshore sands, in *Proceedings of 15th Coastal Engineering Conference*, pp. 2109-2126, American Society of Civil Engineers, New York, 1977.
- Downing, J. P., R. W. Sternberg, and C. R. B. Lister, New instrumentation for the investigation of sediment suspension processes in the shallow marine environment, *Mar. Geol.*, **42**, 19-34, 1981.
- Dyer, K. R., and R. L. Soulsby, Sand transport on the continental shelf, *Annu. Rev. Fluid Mech.*, **20**, 295-324, 1988.
- Grant, W. D., and O. S. Madsen, Combined wave and current interaction with a rough bottom, *J. Geophys. Res.*, **84**(C4), 1797-1808, 1979.
- Grant, W. D., and O. S. Madsen, The continental shelf bottom boundary layer, *Annu. Rev. Fluid Mech.*, **18**, 265-305, 1986.
- Greenwood, B., and P. R. Mittler, Structural indices of sediment transport in a straight, wave-formed, nearshore bar, *Mar. Geol.*, **32**, 191-203, 1979.
- Guza, R. T., and E. B. Thornton, Local and shoaled comparisons of sea surface elevations, pressures, and velocities, *J. Geophys. Res.*, **85**(C3), 1524-1530, 1980.
- Hanes, D. M., C. E. Vincent, D. A. Huntley, and T. L. Clarke, Acoustic measurements of suspended sand concentration in the C²S² experiment at Stanhope Lane, Prince Edward Island, *Mar. Geol.*, **81**, 185-196, 1988.
- Hay, A. E., Sound scattering from a particle-laden turbulent jet, *J. Acoust. Soc. Am.*, **90**(4), 2055-2074, 1991.
- Hay, A. E., and J. Sheng, Vertical profiles of suspended sand concentration and size from multifrequency acoustic backscatter, *J. Geophys. Res.*, **97**(C10), 15,661-15,677, 1992.
- Hay, A. E., L. Huang, E. B. Colburne, J. Sheng, and A. J. Bowen, A high-speed multichannel data acquisition system for remote acoustic sediment transport studies, in *Proceedings of Oceans '88*, pp. 413-418, Marine Technology Society, Washington, D. C., 1988.
- Hazen, D. G., D. A. Huntley, and A. J. Bowen, UDATS: A system for measuring nearshore processes, in *Proceedings of Oceans '87*, pp. 993-997, Marine Technology Society, Washington, D. C., 1987.
- Hess, F. R., and K. W. Bedford, Acoustic backscatter system (ABSS): The instrument and some preliminary results, *Mar. Geol.*, **6**, 357-380, 1985.
- Horikawa, K. (Ed.), *Nearshore Dynamics and Coastal Processes*, 522 pp., University of Tokyo Press, Tokyo, 1988.
- Horikawa, K., A. Watanabe, and S. Katori, Sediment transport under sheet flow condition, in *Proceedings of 18th Coastal Engineering Conference*, pp. 1335-1352, American Society of Civil Engineers, New York, 1982.
- Hunter, R. E., H. E. Clifton, and R. L. Phillips, Depositional processes, sedimentary structures, and predicted vertical sequences in barred nearshore systems, Southern Oregon Coast, *J. Sediment. Petrol.*, **49**, 711-726, 1979.
- Inman, D. L., Wave generated ripples in nearshore sands, *Tech. Memo. 100*, 65 pp., Beach Erosion Board, U.S. Army Corps of Eng., Vicksburg, Miss., 1957.
- Jonsson, I. G., Wave boundary layers and friction factors, in *Proceedings of 10th Coastal Engineering Conference*, pp. 127-148, American Society of Civil Engineers, New York, 1966.
- Kraus, N. C., and K. Horikawa, Nearshore sediment transport, in *The Sea*, vol. 9, part B, edited by B. Le Méhauté and D. M. Hanes, pp. 775-813, John Wiley, New York, 1990.
- Large, W. G., and S. Pond, Open ocean momentum flux measurements in moderate to strong winds, *J. Phys. Oceanogr.*, **11**, 324-336, 1981.
- Large, W. G., and S. Pond, Sensible and latent heat flux measurements over the ocean, *J. Phys. Oceanogr.*, **12**, 464-482, 1982.
- Lynch, J. F., and Y. C. Agrawal, A model-dependent method for

- inverting vertical profiles of scattering to obtain particle size spectra in boundary layers, *Mar. Geol.*, 99, 387-401, 1991.
- Lynch, J. F., T. F. Gross, C. Libiciki, and K. W. Bedford, Deepwater sediment concentration profiling in HEBBLE using a one megahertz acoustic backscatter system, in *Coastal Sediments '87*, pp. 250-259, American Society of Civil Engineers, New York, 1987.
- MacKenzie, K. V., Nine-term equation for sound speed in the ocean, *J. Acoust. Soc. Am.*, 70, 807-812, 1981.
- Madsen, O. S., and W. D. Grant, Quantitative description of sediment transport by waves, in *Proceedings of 15th Coastal Engineering Conference*, pp. 1093-1112, American Society of Civil Engineers, New York, 1977.
- McLean, S. R., Turbulence and sediment transport measurements in a North Sea tidal inlet (The Jade), in *North Sea Dynamics*, edited by J. Sundermann and W. Lenz, pp. 436-452, Springer-Verlag, New York, 1983.
- Miller, M. C., and P. D. Komar, A field investigation of the relationship between oscillation ripple spacing and near-bottom wave orbital motions, *J. Sediment. Petrol.*, 50, 183-191, 1980.
- Mimura, N., Y. Ohtsuka, and A. Watanabe, Laboratory study on two-dimensional beach transformation due to irregular waves, in *Proceedings of 20th Coastal Engineering Conference*, pp. 1393-1406, American Society of Civil Engineers, New York, 1987.
- Nielsen, P., Some basic concepts of wave sediment transport, *Ser. Pap. 20*, Inst. of Hydrodyn. and Hydraul Eng., Tech. Univ. of Denmark, Lyngby, 1979.
- Nielsen, P., Dynamics and geometry of wave-generated ripples, *J. Geophys. Res.*, 86(C7), 6467-6472, 1981.
- Ogilvy, J. A., *Theory of Wave Scattering from Random Rough Surfaces*, 277 pp., Adam Hilger, Bristol, England, 1991.
- Sleath, J. F. A., The suspension of sand by waves, *J. Hydraul. Res.*, 20, 439-452, 1982.
- Sleath, J. F. A., *Sea Bed Mechanics*, 335 pp., John Wiley, New York, 1984.
- Sternberg, R. W., Measurements of sediment movement and ripple migration in shallow marine environment, *Mar. Geol.*, 5, 195-205, 1967.
- Thorne, P. D., C. E. Vincent, P. J. Hardcastle, S. Rehman, and N. Pearson, Measuring suspended sediment concentrations using acoustic backscatter, *Mar. Geol.*, 98, 7-16, 1991.
- Vincent, C. E., R. A. Young, and D. J. P. Swift, Bed-load transport under waves and currents, *Mar. Geol.*, 39, 71-80, 1981.
- Vincent, C. E., D. M. Hanes, and A. J. Bowen, Acoustic measurements of suspended sand on the shoreface and the control of concentration by bed roughness, *Mar. Geol.*, 96, 1-18, 1991.
- Watanabe, A., Numerical simulation of nearshore current and beach transformation, in *Proceedings of 28th Japanese Conference on Coastal Engineering*, pp. 285-289, Japan Society of Civil Engineers, Tokyo, 1981.
- Watanabe, A., Numerical models of nearshore currents and beach deformation, *Coastal Eng. Jpn.*, 25, 147-161, 1982.
- Young, R. A., J. T. Merrill, T. L. Clarke, and J. R. Proni, Acoustic profiling of suspended sediments in the marine bottom boundary layer, *Geophys. Res. Lett.*, 9, 175-178, 1982.

A. J. Bowen, Department of Oceanography, Dalhousie University, Halifax, Nova Scotia, Canada B3H 4J1.

A. E. Hay, Department of Physics and Ocean Sciences Centre, Memorial University of Newfoundland, St. John's, Newfoundland, Canada A1B 3X7.

(Received May 1, 1992;
revised October 21, 1992;
accepted November 4, 1992.)